

---

# SCRREAM : SCan, Register, REndeR And Map: A Framework for Annotating Accurate and Dense 3D Indoor Scenes with a Benchmark

---

**HyunJun Jung**

Technical University of Munich  
hyunjun.jung@tum.de

**Weihang Li**

Technical University of Munich

**Shun-Cheng Wu**

Technical University of Munich

**William Bittner**

Technical University of Munich

**Nikolas Brasch**

Technical University of Munich

**Jifei Song**

Huawei Noah's Ark Lab

**Eduardo Pérez-Pellitero**

Huawei Noah's Ark Lab

**Zhensong Zhang**

Huawei Noah's Ark Lab

**Arthur Moreau**

Huawei Noah's Ark Lab

**Nassir Navab**

Technical University of Munich

**Benjamin Busam**

Technical University of Munich  
b.busam@tum.de

## Abstract

Traditionally, 3d indoor datasets have generally prioritized scale over ground-truth accuracy in order to obtain improved generalization. However, using these datasets to evaluate dense geometry tasks, such as depth rendering, can be problematic as the meshes of the dataset are often incomplete and may produce wrong ground truth to evaluate the details. In this paper, we propose SCRREAM, a dataset annotation framework that allows annotation of fully dense meshes of objects in the scene and registers camera poses on the real image sequence, which can produce accurate ground truth for both sparse 3D as well as dense 3D tasks. We show the details of the dataset annotation pipeline and showcase four possible variants of datasets that can be obtained from our framework with example scenes, such as indoor reconstruction and SLAM, scene editing & object removal, human reconstruction and 6d pose estimation. Recent pipelines for indoor reconstruction and SLAM serve as new benchmarks. In contrast to previous indoor dataset, our design allows to evaluate dense geometry tasks on eleven sample scenes against accurately rendered ground truth depth maps.

## 1 introduction

Indoor tasks are heavily related to human activities. As a consequence, perceiving 3D indoor scenes is one of the major tasks in 3D computer vision. A series of indoor datasets [1–8] with different annotation methods has been introduced to the vision community to provide the data necessary for training and for performance evaluation. Such datasets, however, are generally capturing a scene with a depth sensor from a limited number of viewpoints, trying to avoid making any changes to the scene



Figure 1: Due to the typical acquisition pipelines, traditional indoor 3D datasets can provide incomplete meshes for their scenes with missing structures and holes. Our dataset annotation pipeline, in contrast, starts from scanning individual objects in an high resolution manner and then registers them to the real scene and real camera sequence allowing highly detailed ground truth rendering for dense 3D vision tasks.

to simplify registration and fusion. While this way of scanning can speed up the dataset capturing process and allows for fast large scale data creation, it has the drawback of potentially acquiring incomplete meshes due to e.g. line of sight problems or lack of sensor accuracy.

On the other hand, [9] showed that scanning all objects individually and consecutively registering them into the scene can ensure dense and complete annotations for all objects. In turn, they can be used to render dense ground truth. However, using a robotic arm limits the scene setup as well as the camera trajectory to scenarios such as table-top scenes with cameras that cannot move freely due to the robot’s limited joint operation range. Therefore we design a novel pipeline that replaces the tool tip based object registration with a highly accurate partial re-scan and registration procedure. We adapted feature matching based pose estimation leveraging synthetic views rendered from the registered model similar to [7] to replace external hardware based camera tracking (see Fig. 1).

Due to the flexibility of the approach to scan and annotate scenes for different purposes, we refer to it as a framework. It can be used for various tasks such as indoor reconstruction & SLAM, scene editing & object removal, human reconstruction and 6d pose estimation. In later sections, we detail the steps of the framework and discuss how the scene can be setup to obtain different variants of indoor datasets. To showcase the versatility of the framework we provide eleven example scenes obtained using the proposed framework. The entire dataset is made available for the community<sup>1</sup> and we provide a benchmark for 3D geometric tasks using existing state of the art (SoTA) methods for indoor reconstruction & SLAM on our example scenes.

To this end, our contributions are :

1. We propose a dataset annotation framework that is capable of annotating fully dense indoor scenes. It can be applied to different indoor perception tasks.
2. We detail the steps of our annotation framework for future use and release an acquired dataset into the public domain with detailed documentation.
3. We create a new benchmark for scene level geometry tasks comprising indoor scene reconstruction, novel view synthesis and SLAM using accurately rendered dense depth ground truth as well as precise meshes.

## 2 Related Works

Early datasets obtain their annotations by using directly the depth sensor readings [1, 2], where invalid or empty pixels are manually annotated to provide dense 3D data for evaluation [1]. Later, the paradigm for annotation changed, i.e. the indoor scene is reconstructed by fusing a sequence of depth images obtained by multi modal camera trajectories [3–5] to produce more complete scene geometry. Depth and other 3d information is produced on the image plane by rendering the mesh using the camera pose. To improve the quality and density of the datasets, annotation methods that pre-scan the scene, record [6] and localize the camera are developed [7, 8]. Although this annotation technique

<sup>1</sup>Dataset link and toolkit can be found in <https://github.com/Junggy/SCRREAM>

Table 1: **Dataset Comparison.** Each scene in our dataset is annotated with individually scanned water-tight high resolution meshes with texture maps which are provided as digital twin assets. Thus, fully dense ground truth maps such as highly detailed depth and instance/class segmentation maps can be rendered. This serves as accurate benchmark data. We additionally provide scenes with reduced objects in the scene to provide object removal and scene editing setup that comprises of extra 9k frames.

Dataset	Real Data	RGB Sequence	Polarization	Camera Pose	Scene Reconstruction Mesh	Digital Twin Asset	Class Segmentation	Instance Segmentation	Scene Editability	Free-Hand Camera	Accurate Depth GT	Photogrammetry Depth	Structured Light Depth	ToF Depth	Active Stereo Depth	Number of Scenes	Number of Frames
NYU [1]	✓	✓					✓			✓						464	1449
TUM RGBD [2]	✓	✓		✓						✓		✓				6	> 10k
ScanNet [3]	✓	✓		✓	✓		✓			✓		✓				1513	2.5M
Matterport3D [4]	✓	✓		✓	✓		✓					✓				2056	194k
Stanford2D-3D [5]	✓	✓		✓	✓		✓					✓				25	70k
Replica [6]	✓				✓		✓					-	-	-	-	18	N/A
ReplicaCAD [10]					✓	✓	✓	✓	✓			-	-	-	-	111	N/A
RoboTHOR [11]					✓	✓	✓	✓	✓			-	-	-	-	89	N/A
HAMMER [9]	✓	✓	✓	✓	✓	✓	✓	✓			✓			✓		13	> 10k
ARKitScenes [8]	✓	✓		✓	✓		✓			✓				✓		1661	450k
ScanNet++ [7]	✓	✓		✓	✓		✓			✓				✓		5047	3.7M
Ours	✓	✓	✓	✓	✓	✓	✓	✓	✓	✓	✓			✓	✓	11	7k(+9k)

produces a significantly better mesh quality of the scene, it suffers from line of sight problems of the scanner as the scanning is done on a scene level. Ensuring every single object in the scene is complete is a non-trivial task. As a result, dense ground truth generated in this way suffers from holes and missing parts. Therefore, scene-level reconstruction methods like neural radiance fields (NeRF) [12] variants or 3D Gaussian Splatting [13] evaluate their geometry only via qualitative evaluation on their depth prediction.

To ensure complete scenes, [10, 11] proposed synthetic data with high-quality CAD models created by artists. ReplicaCAD [10] proposed a synthetic version of Replica dataset [6] that contains room of Replica dataset but with different layouts with CAD models. Similarly, the RoboThor dataset creates a modular room that contains different layouts from CAD models based on IKEA furniture. These approaches ensure the scene’s completeness and the dataset’s scale. However, as the aim of the dataset is instead a robotic simulation, the data is not focused on realism and thus suffers from sym and real domain gaps. HAMMER [9] constitutes an annotation method that uses a robotic arm to annotate pre-scanned meshes as well as a camera trajectory. In contrast to other datasets, all meshes are pre-scanned individually to make sure there is no missing part such that holes in the area of interest cannot occur. This results in annotated scene from which highly accurate depth rendering can be acquired without any artifacts. These can be used as absolute ground truth for depth prediction tasks. However, the robotic arm’s range of motion is limited such that the acquisition process is capable of annotating only table top scenarios with small camera motion. HouseCat6D [14] replaces the robotic arm with an external tracking device for better flexibility and wider camera motion. While it improves both scene and camera pose diversity significantly, the dataset cannot achieve true free hand-held camera trajectories due to line of sight problem of the tracking device. Moreover, the tracking camera set up in the background of the scene makes the dataset less suitable for indoor reconstruction purposes. In this work, we combine the two methods for annotation [9, 14] and [7, 8], and achieve a fully dense annotation pipeline of scenes as well as free hand-held camera trajectories.

### 3 Dataset Acquisition Method

Our goal is to setup a pipeline that is capable of annotating the fully dense scene as well as image sequence recorded by a free hand-held camera with reliable camera poses. Our pipeline follows the **SCRREAM** scheme : **SC**anning the complete meshes, **RE**gistering the meshes to the scene, **RE**nder

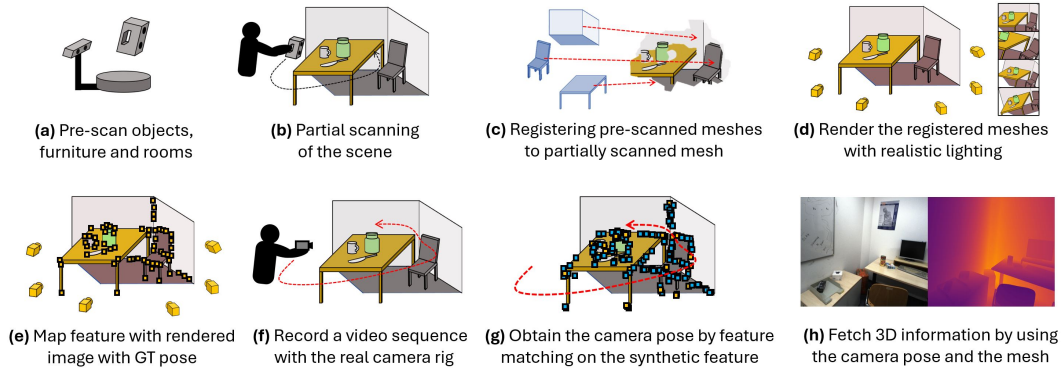


Figure 2: **Framework Pipeline Overview.** Our pipeline follows the SCRREAM scheme for annotation. **(a) SCan** : Scanning the individual objects in the scene, **(b,c) Register** : Place objects in the scene, scan the scene partially and register the pre-scanned meshes, **(d) REnde**r : Render the synthetic images, And **(e-g) Mapping** : Map 3D features of synthetic image with camera poses, record the real image sequence and obtain the camera pose via feature matching. Once the camera poses are obtained, we can extract or render the 3D information via transforming the meshes into the camera frame as shown in **(h)**.

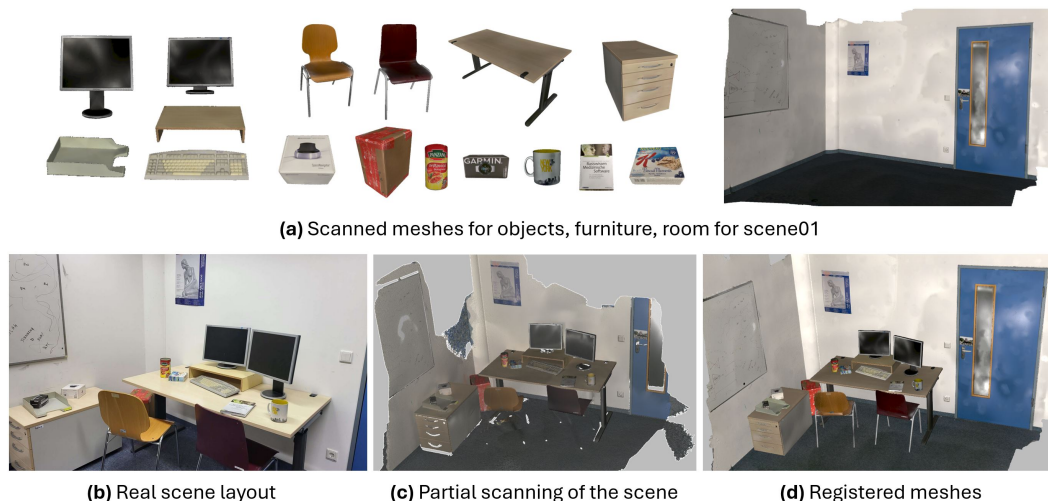


Figure 3: **Example for the Scan and Register Step.** **(a)** We pre-scan all meshes in the scene before setting up the scene. This ensures that all objects and furniture are scanned in a high quality, water-tight manner. **(b)** Then we place the furniture in the room to setup the scene and **(c)** scan the entire scene (Note that the scene is not scanned completely), such that we can **(d)** register all pre-scanned meshes to the scene layout via manual correspondence selection followed by ICP.

the synthetic scene And Mapping the video sequence to a synthetic scene to obtain the camera pose. In this section, we explain in more detail each part of the SCRREAM pipeline.

**Scan.** In the scanning step, we scan the entire empty room, furniture and small objects in the scene separately to obtain the complete meshes such that all the objects and furniture in the scenes are complete regardless of line of sight of the scanner or camera trajectory. We use an EinScan-SP (SHINING 3D) for scanning small household objects and an Artec Leo (Artec 3D) for scanning the furniture and room. For the small household objects and furniture, we make sure the scanned meshes are water tight and have high quality texture maps. The scanning step corresponds to Fig. 2 (a) in the pipeline, and examples for scanned meshes are shown in Fig. 3 (a).

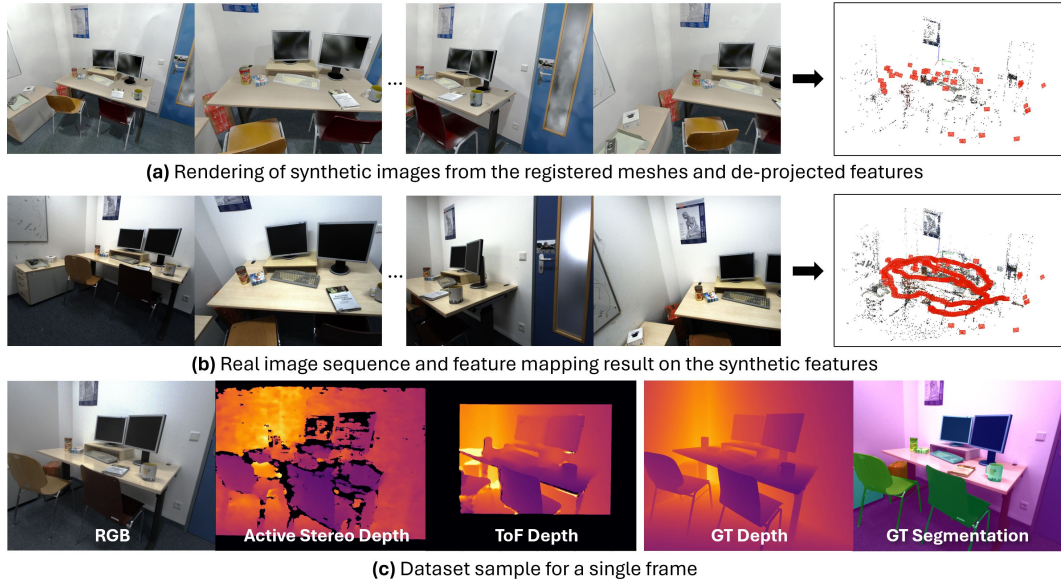


Figure 4: **Example for the Mapping Step and Qualitative Evaluation.** Mapping starts with (a) generating realistic synthetic renderings from the registered mesh. Once the images are rendered, features are matched and de-projected to 3D. Then (b) the real sequence is acquired, and features are extracted to match with synthetic features to obtain the camera poses. These camera poses allow us to transform the camera frame to the mesh frame such that dense 3D annotations (c) can be rendered into the image as ground truth. We show rendered instance masks as well as depth on the real image frame to illustrate the quality of our ground truth.

**Register.** Once the scanning is done for all objects, the furniture and room, we create the scene by placing the furniture and objects in the room. The scene is then scanned as a whole with the hand-held scanner to provide the sparse mesh that can be used to register the pre-scanned meshes to the scene similar to [9]. Initial registration is done by selecting 3-5 pairs of corresponding points between the pre-scanned mesh and the sparse mesh. This is further refined using ICP [15]. The register step corresponds to Fig. 2 (b),(c). An example of a partial scan and the corresponding registered meshes can be found in Fig. 3 (c),(d). For convenience, we use a commercial software (Artec Studio 17 Professional) for this registration step.

**Render.** The registered scene with the pre-scanned meshes are then used to render the scene in a realistic manner. We use Blender4.0 [16] for rendering the scene by importing all registered meshes and placing the light source close to the real scene. We render around 50-100 frames that can cover many views of the scene that can be used for the next mapping step and save the corresponding camera poses and intrinsics as a pair. The rendering step corresponds to Fig. 2 (d). Examples of rendered images are shown in Fig. 4 (a).

**Mapping.** The mapping stage maps the real image sequence to the rendered sequence that is obtained by the previous step. To obtain the real image sequence of the scene, we use a multi-modal camera rig that is composed of an RGB+P sensor (Lucid Phoenix with Sony Polarsens), an active stereo depth sensor (intel RealSense D435) and an I-ToF depth sensor (Lucid Helios). Extrinsic calibration is obtained from each depth sensor to the RGB sensor using the calibration scheme similar to [14]. We first place a ChArUco board and capture image sequences from all cameras to obtain sequences with trajectories  $T_{camX \rightarrow board}$ . For depth sensors, infra-red images are used to capture the ChArUco board. Then we align the trajectories from Depth sensors to RGB sensor using Horn’s method [17]. The alignment matrix is an extrinsic matrix between RGB and the depth sensor. Once the extrinsic matrices are obtained from each depth sensor to the RGB sensor, the corresponding depth image is aligned to the RGB image using its own sensor depth and their extrinsic. Note that we use noisy sensor depth to align depth images to the RGB image, which leads extra noises in the final depth image. We design this way specifically as this is how the real depth sensor produces an aligned depth

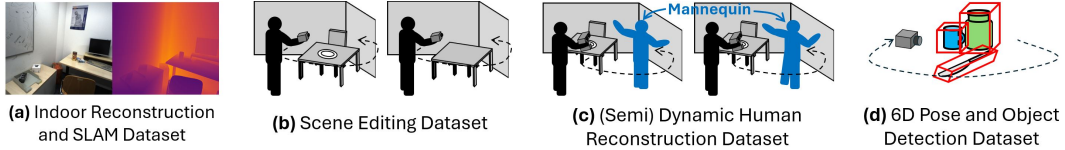


Figure 5: **Dataset Variation Overview.** Depending on the scene setup, our annotation framework can produce different variants of ground truth. (a) rendering depth for indoor reconstruction and SLAM; (b) capturing scene with less objects produces ground truth for scene editing; (c) capturing scene with a mannequin in stop-motion for semi dynamic human reconstruction; (d) capturing a 360-degree video around the objects for a 6D pose and detection dataset.

image to its RGB image. All three cameras are synchronized by a hardware sync signal generated via a Raspberry Pi. We include more hardware details in the supplementary material.

Once the real image sequence is obtained, our task is to obtain the camera pose relative to the center of the registered scene meshes. We modify the off-the-shelf Structure from Motion (SfM) method COLMAP [18, 19] into two stages (two-stage mapping) to obtain the real camera poses from the synthetic images paired with camera pose and intrinsics. We first match the features from synthetic images and de-project them into 3D by using the paired camera poses and intrinsics. We then extract features of real images and match them to the synthetic image features and the corresponding camera poses are optimized to map the de-projected real image features onto de-projected synthetic features. The mapping step corresponds to Fig. 2 (e)-(g). An example of a real image sequence and mapped features with the retrieved camera pose is shown in Fig. 4 (b).

When the camera pose is obtained, we can map the available 3D information onto the camera frame by using the camera pose and meshes to annotate the scene frames with, e.g. dense depth (see Fig. 2 (h)), object poses, segmentation masks, surface normals, bounding boxes etc. We show possible variations of the dataset acquisition with the SCRREAM annotation framework in Sec. 4.

## 4 Dataset Variations

Our SCRREAM annotation framework is specialized in annotating fully dense meshes of a given scene with a freely moving camera. Depending on how the scene is set up, our pipeline can be used to annotate ground truth on data for different types of tasks (Fig. 5), such as indoor reconstruction and SLAM, object removal and scene editing, human reconstruction and 6D pose estimation. For each of the four variants, we provide publicly available data and provide detailed documentation in the supplementary material.

**Indoor Reconstruction and SLAM Dataset.** In this part, we consider indoor reconstruction and SLAM as the major task of our dataset. The dataset can be obtained by following the annotation pipeline described above. Dense depth maps and instance masks are rendered with camera poses and annotated meshes of the scene as shown in Fig. 4 (c). We acquire **eleven scenes** for this task and provide the benchmarks that evaluate the quality of view synthesis and 3D geometry tasks using recent approaches in Sec. 5.

**Object Removal & Scene Editing Dataset.** Object removal and scene editing datasets can be created by capturing the scene multiple times with less objects appearing in the scene (reduced scene). The advantage of using our pipeline is that one can easily exclude the object meshes that need to be removed from the scene and render the correct depth to evaluate the geometry. Also running the mapping on both camera trajectories with and without the target objects ensures both camera poses to be using the same reference. We recorded extra trajectories in this reduced setup for **eight selected scenes** from the eleven Indoor Reconstruction and SLAM Dataset scenes. Examples are shown in Fig. 6 (a).

**Human Reconstruction Dataset.** Human reconstruction datasets can be divided into two categories based on their capture setup. While the first set of datasets captures the human in a motion capture setup [20–22] (i.e. a static multi-camera recording studio with a human performer in the middle), the second acquisition setup focuses on real scenes with changing backgrounds and uses a simple hand-

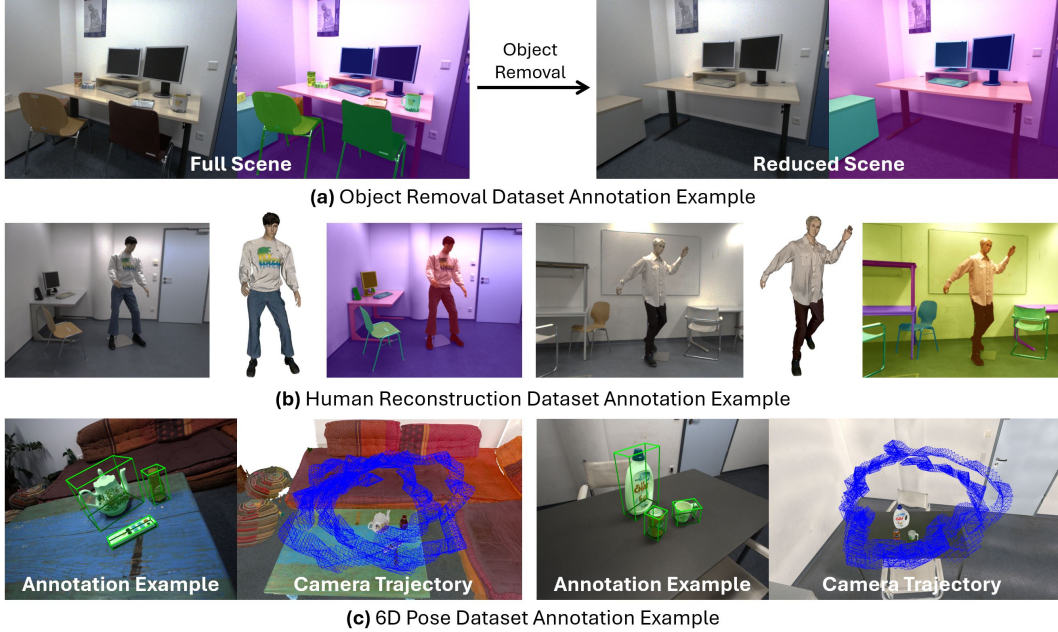


Figure 6: **Dataset Variation Example.** (a) Our scene editing and object removal dataset provides mask and geometry annotation with and without the selected objects. (b) Our human reconstruction dataset is semi-dynamic using a stop motion mannequin, but each frame is fully scanned to provide the high quality reconstruction ground truth. (c) The 6D pose dataset from our pipeline can produce high quality annotation and 360 degree view of objects without any markers.

held camera [23] that can also be used outdoors. The former datasets have the advantage of being capable of capturing high quality annotation, but they lack realism in the scene as the background is the camera acquisition sphere. The latter lack the accuracy while they have the advantage of a realistic background. In our case, we use a mannequin with multiple joints to create a stop motion video, but scan and annotate the mannequin each frame with our annotation pipeline. This allows to create a human dataset that contains realistic backgrounds as well as high quality mesh annotations for both background and human. **Two sample scenes** are collected to showcase the high quality human annotation on each frame in the sequence as well as the realism of the background. We also annotated SMPL [24] parameters using the RVH Mesh registration repository [25, 26]. Example scenes are shown in Fig. 6 (b).

**6D Pose Estimation Dataset.** By nature of our annotation, the pipeline co-stores object poses and camera trajectories from the scene origin. Concatenating the two poses in the right order produces 6D object pose in camera coordinates. Using our pipeline allows for better camera coverage (e.g. 360 deg trajectories) compared to external tracking based pipelines like Hammer [9] or PhoCal [27] and more realistic scenes overcome the need of markers [28, 29]. We collect **two example scenes** to showcase the possible use of our pipeline. Examples are shown in Fig. 6 (c).

## 5 Benchmarks

In this section, we provide a benchmark for the two arguably most popular scene-level (e.g. train and test on the same scene) indoor 3D vision task, namely SLAM and Novel View Synthesis. We run all experiments on a RTX 4090 GPU and an i9 13th Gen CPU and show the result averaged over all scenes. Results on individual scenes can be found in the supplementary material.

**Novel View Synthesis Geometry Benchmarks.** We select four SoTA Novel View Synthesis (NVS) methods and depth supervision variants for a benchmark. We use NerFacto [30] with and without depth prior (Depth-Facto with two depth sensor priors), Zip-NeRF [31], Gaussian-Splatting [13] and Mip-Splatting [32]. Unlike any existing NVS benchmarks, our dataset provides highly detailed

Table 2: **Quantitative Evaluation for Novel View Synthesis.** In addition to the photometric evaluation (RGB), our indoor benchmark provides ground truth depth. This allows the evaluation on the rendered depth to study each method’s performance on the geometric reconstruction (depth). We differentiate between NeRF methods (upper part) and Gaussian Splatting methods (lower part).

Evaluation	RGB			Depth					
	PSNR $\uparrow$	SSIM $\uparrow$	LPIPS $\downarrow$	RSME $\downarrow$	Abs Rel $\downarrow$	Sqr Rel $\downarrow$	$<1.25^1 \uparrow$	$<1.25^2 \uparrow$	$<1.25^3 \uparrow$
NeRFacto [30]	22.645	0.765	0.343	1.244	0.645	1.231	0.429	0.597	0.726
Depth-Facto [30] (AS)	24.502	0.786	0.324	<b>0.218</b>	<b>0.079</b>	<b>0.059</b>	<b>0.968</b>	<b>0.981</b>	<b>0.988</b>
Depth-Facto [30] (ToF)	24.540	0.788	0.323	0.336	0.093	0.149	0.926	0.943	0.957
Zip-NeRF [31]	<b>28.315</b>	0.783	<b>0.259</b>	0.493	0.245	0.189	0.546	0.825	0.887
Gaussian-Splatting [13]	25.943	0.801	0.328	0.526	0.218	0.174	0.589	0.806	0.883
Mip-Splatting [32]	25.925	<b>0.802</b>	0.327	0.532	0.223	0.178	0.594	0.794	0.875

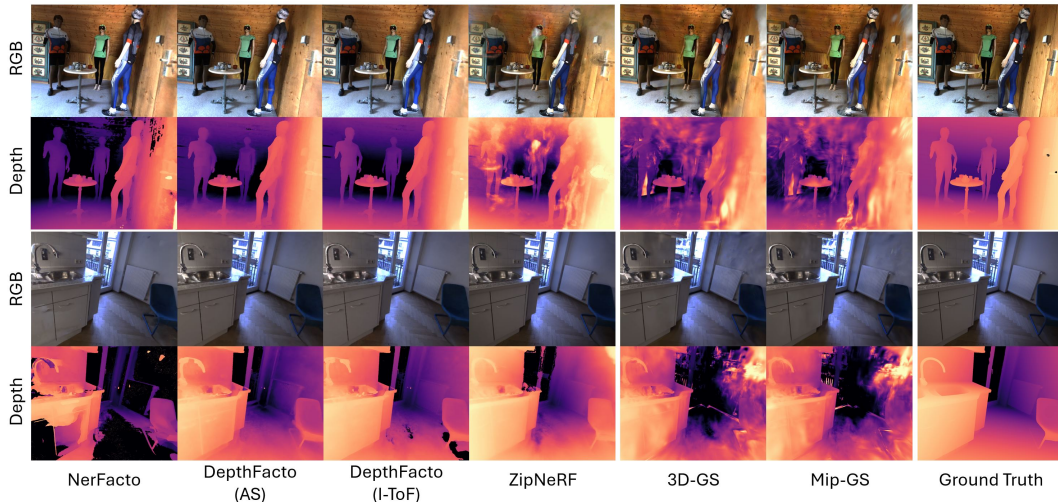


Figure 7: **Qualitative Evaluation of NVS Baselines.** We show rendering results of NeRF (NerFacto/DepthFacto, ZipNeRF) and Gaussian Splatting (3D-GS, Mip-GS) methods for both RGB and depth. The results show that realistic photometric appearance (RGB) does not always coincide with high quality depth rendering, while using sensor depth significantly improves the geometric understanding regardless of its modality. This indicates a larger room to improve geometric scene understanding with recent methods to allow for realistic real world vision application, such as Virtual Reality or Augmented Reality. Zoom in for details.

rendered ground truth depth without missing parts on the objects. This allows to further provide the evaluation metric on the depth rendering (i.e. RMSE, Abs Rel, Sqr Rel,  $\delta < 1.25^n$ ) to evaluate the geometric cue for each method together with traditional view synthesis metrics, such as PSNR, SSIM, LPIPS [33]. We use every 10th frame for training and the in between frame (every 10th frame + 5) for testing. Quantitative and qualitative evaluations are shown in Tab. 2 and Fig. 7.

**Indoor SLAM Benchmarks.** For SLAM, we select three SoTA RGB-D SLAM methods as benchmark, namely NICE-SLAM [34], CO-SLAM [35] and Gaussian-SLAM [36]. As aforementioned SLAM methods require depth as input, we run experiments on two sensor depths, Active Stereo and ToF, to evaluate the performance on a real-life scenario, as well as on rendered ground truth depth to understand the maximum possible performance of each method in the best case scenario. We use all frames to train and evaluate the obtained camera pose and scene reconstruction. Tracking performance is evaluated by absolute trajectory error (ATE) and RMSE [37]. Mapping performance is assessed using three common metrics for Neural RGB-D SLAM [38, 34, 35]: Accuracy, Completion, and Completion Ratio. Before mesh evaluation, unseen and occluded regions are culled using the strategy proposed in [39]. Quantitative and qualitative evaluations are shown in Tab. 3 and Fig. 8.



Table 3: **Quantitative Evaluation of SLAM.** We benchmark three SoTA RGB-D SLAM methods, namely NICE-SLAM, CO-SLAM, and Gaussian-SLAM. We use an Active Stereo depth sensor (AS) and a ToF sensor (ToF) as well as the ground truth depth (GT) input to test the upper limit of each method.

Evaluation		Tracking		Mapping	
Methods	Depth	ATE↓ [cm]	Acc↓ [cm]	Comp↓ [cm]	Comp Ratio↑ [%]
NICE-SLAM [34]	AS	39.09	23.64	14.51	37.49
	ToF	24.02	21.60	14.63	46.18
	GT	5.47	2.91	5.91	77.11
CO-SLAM [35]	AS	39.19	32.38	12.95	40.07
	ToF	45.94	58.22	8.02	57.68
	GT	4.18	1.87	1.69	96.52
Gaussian-SLAM [36]	AS	38.20	37.94	11.74	41.36
	ToF	83.53	43.67	9.06	53.79
	GT	5.00	2.25	1.70	94.89

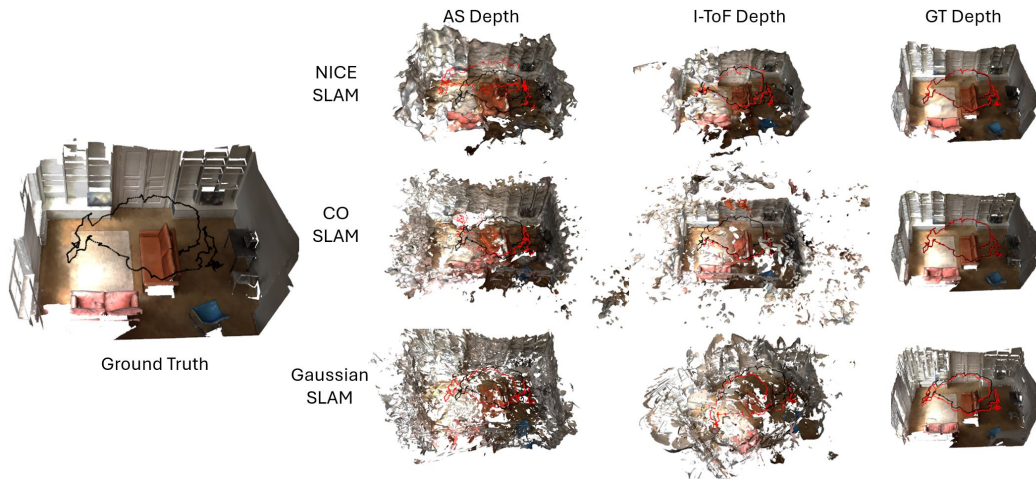


Figure 8: **Qualitative Evaluation of SLAM Methods.** Results of the 3 SoTA SLAM pipelines are shown as camera trajectory and scene reconstruction results. Each predicted camera trajectory (red) is compared with the ground truth camera trajectory (black). Zoom in for details.

## 6 Limitation and Conclusion

SCRREAM constitutes an indoor 3D dataset annotation framework capable of annotating individual high quality scene meshes. We exemplify its use for annotation of four different tasks for which we provide example datasets. Furthermore, benchmarks on the reconstruction and SLAM dataset using most recent methods are given. While the scene annotation is more detailed, the used hardware setup might be expensive, complex, and time-consuming, making the dataset annotation pipeline less scalable; for human reconstruction, 6d pose estimation dataset, we only include a few sample dataset scenes without benchmarks on the corresponding topics. To make individual images most comparable, we opted for a fixed exposure time which can cause under/over-exposed images and motion blur in darker scenes. Using a feature-based matching and pose estimation method requires static capturing conditions to ensure highly accurate camera pose estimation during the annotation stage. This limits the scene editing setup we propose is only capable of removing objects, not actual human interaction involved [40]. Limited by the scanning speed, we use mannequins instead of real humans that lack motions and realism, especially in the face and hand areas. Regardless of these drawbacks, our dataset is the only dataset to our knowledge with such an accurate setup covering the indoor room with a hand-held camera. This uniquely allows in-depth geometric evaluation and benchmarking of methods for most popular 3D applications such as NVS and SLAM. We strongly believe that our dataset and benchmark can bring forward the field through objective evaluation and public access for the research community by not simply taking sensor depth granted ground truth.

## References

- [1] P. K. Nathan Silberman, Derek Hoiem and R. Fergus, “Indoor segmentation and support inference from rgb-d images,” in *ECCV*, 2012.
- [2] J. Sturm, N. Engelhard, F. Endres, W. Burgard, and D. Cremers, “A benchmark for the evaluation of rgb-d slam systems,” in *Proc. of the International Conference on Intelligent Robot Systems (IROS)*, Oct. 2012.
- [3] A. Dai, A. X. Chang, M. Savva, M. Halber, T. Funkhouser, and M. Nießner, “Scannet: Richly-annotated 3d reconstructions of indoor scenes,” in *Proc. Computer Vision and Pattern Recognition (CVPR), IEEE*, 2017.
- [4] A. Chang, A. Dai, T. Funkhouser, M. Halber, M. Niessner, M. Savva, S. Song, A. Zeng, and Y. Zhang, “Matterport3d: Learning from rgb-d data in indoor environments,” *International Conference on 3D Vision (3DV)*, 2017.
- [5] I. Armeni, A. Sax, A. R. Zamir, and S. Savarese, “Joint 2D-3D-Semantic Data for Indoor Scene Understanding,” *ArXiv e-prints*, Feb. 2017.
- [6] J. Straub, T. Whelan, L. Ma, Y. Chen, E. Wijmans, S. Green, J. J. Engel, R. Mur-Artal, C. Ren, S. Verma, A. Clarkson, M. Yan, B. Budge, Y. Yan, X. Pan, J. Yon, Y. Zou, K. Leon, N. Carter, J. Briales, T. Gillingham, E. Mueggler, L. Pesqueira, M. Savva, D. Batra, H. M. Strasdat, R. D. Nardi, M. Goesele, S. Lovegrove, and R. Newcombe, “The Replica dataset: A digital replica of indoor spaces,” *arXiv preprint arXiv:1906.05797*, 2019.
- [7] C. Yeshwanth, Y.-C. Liu, M. Nießner, and A. Dai, “Scannet++: A high-fidelity dataset of 3d indoor scenes,” in *Proceedings of the IEEE/CVF International Conference on Computer Vision*, 2023, pp. 12–22.
- [8] G. Baruch, Z. Chen, A. Dehghan, T. Dimry, Y. Feigin, P. Fu, T. Gebauer, B. Joffe, D. Kurz, A. Schwartz *et al.*, “ArkitScenes: A diverse real-world dataset for 3d indoor scene understanding using mobile rgb-d data,” *arXiv preprint arXiv:2111.08897*, 2021.
- [9] H. Jung, P. Ruhkamp, G. Zhai, N. Brasch, Y. Li, Y. Verdie, J. Song, Y. Zhou, A. Armagan, S. Ilic, A. Leonardis, N. Navab, and B. Busam, “On the importance of accurate geometry data for dense 3d vision tasks,” in *Proceedings of the IEEE/CVF Conference on Computer Vision and Pattern Recognition (CVPR)*, June 2023, pp. 780–791.
- [10] A. Szot, A. Clegg, E. Undersander, E. Wijmans, Y. Zhao, J. Turner, N. Maestre, M. Mukadam, D. Chaplot, O. Maksymets, A. Gokaslan, V. Vondrus, S. Dharur, F. Meier, W. Galuba, A. Chang, Z. Kira, V. Koltun, J. Malik, M. Savva, and D. Batra, “Habitat 2.0: Training home assistants to rearrange their habitat,” in *Advances in Neural Information Processing Systems (NeurIPS)*, 2021.
- [11] M. Deitke, W. Han, A. Herrasti, A. Kembhavi, E. Kolve, R. Mottaghi, J. Salvador, D. Schwenk, E. VanderBilt, M. Wallingford *et al.*, “Robothor: An open simulation-to-real embodied ai platform,” in *Proceedings of the IEEE/CVF conference on computer vision and pattern recognition*, 2020, pp. 3164–3174.
- [12] B. Mildenhall, P. P. Srinivasan, M. Tancik, J. T. Barron, R. Ramamoorthi, and R. Ng, “Nerf: Representing scenes as neural radiance fields for view synthesis,” *Communications of the ACM*, vol. 65, no. 1, pp. 99–106, 2021.
- [13] B. Kerbl, G. Kopanas, T. Leimkühler, and G. Drettakis, “3d gaussian splatting for real-time radiance field rendering,” *ACM Transactions on Graphics*, vol. 42, no. 4, July 2023. [Online]. Available: <https://repo-sam.inria.fr/fungraph/3d-gaussian-splatting/>
- [14] H. Jung, G. Zhai, S.-C. Wu, P. Ruhkamp, H. Schieber, G. Rizzoli, P. Wang, H. Zhao, L. Garattoni, S. Meier, D. Roth, N. Navab, and B. Busam, “Housecat6d – a large-scale multi-modal category level 6d object perception dataset with household objects in realistic scenarios,” in *Proceedings of the IEEE/CVF Conference on Computer Vision and Pattern Recognition (CVPR)*, June 2024.
- [15] K. S. Arun, T. S. Huang, and S. D. Blostein, “Least-squares fitting of two 3-d point sets,” *IEEE Transactions on Pattern Analysis and Machine Intelligence*, vol. PAMI-9, no. 5, pp. 698–700, 1987.
- [16] B. O. Community, *Blender - a 3D modelling and rendering package*, Blender Foundation, Stichting Blender Foundation, Amsterdam, 2018. [Online]. Available: <http://www.blender.org>
- [17] B. K. Horn, H. M. Hilden, and S. Negahdaripour, “Closed-form solution of absolute orientation using orthonormal matrices,” *Josa a*, vol. 5, no. 7, pp. 1127–1135, 1988.
- [18] J. L. Schönberger and J.-M. Frahm, “Structure-from-motion revisited,” in *Conference on Computer Vision and Pattern Recognition (CVPR)*, 2016.

- [19] J. L. Schönberger, E. Zheng, M. Pollefeys, and J.-M. Frahm, “Pixelwise view selection for unstructured multi-view stereo,” in *European Conference on Computer Vision (ECCV)*, 2016.
- [20] S. Peng, Y. Zhang, Y. Xu, Q. Wang, Q. Shuai, H. Bao, and X. Zhou, “Neural body: Implicit neural representations with structured latent codes for novel view synthesis of dynamic humans,” in *CVPR*, 2021.
- [21] H. Joo, T. Simon, X. Li, H. Liu, L. Tan, L. Gui, S. Banerjee, T. S. Godisart, B. Nabbe, I. Matthews, T. Kanade, S. Nobuhara, and Y. Sheikh, “Panoptic studio: A massively multiview system for social interaction capture,” *IEEE Transactions on Pattern Analysis and Machine Intelligence*, 2017.
- [22] M. Işık, M. Rünz, M. Georgopoulos, T. Khakhulin, J. Starck, L. Agapito, and M. Nießner, “Humanrf: High-fidelity neural radiance fields for humans in motion,” *ACM Transactions on Graphics (TOG)*, vol. 42, no. 4, pp. 1–12, 2023. [Online]. Available: <https://doi.org/10.1145/3592415>
- [23] W. Jiang, K. M. Yi, G. Samei, O. Tuzel, and A. Ranjan, “Neuman: Neural human radiance field from a single video,” 2022. [Online]. Available: <https://arxiv.org/abs/2203.12575>
- [24] M. Loper, N. Mahmood, J. Romero, G. Pons-Moll, and M. J. Black, “SMPL: A skinned multi-person linear model,” *ACM Trans. Graphics (Proc. SIGGRAPH Asia)*, vol. 34, no. 6, pp. 248:1–248:16, Oct. 2015.
- [25] B. L. Bhatnagar, C. Sminchisescu, C. Theobalt, and G. Pons-Moll, “Combining implicit function learning and parametric models for 3d human reconstruction,” in *European Conference on Computer Vision (ECCV)*. Springer, aug 2020.
- [26] ———, “Loopreg: Self-supervised learning of implicit surface correspondences, pose and shape for 3d human mesh registration,” in *Advances in Neural Information Processing Systems (NeurIPS)*, December 2020.
- [27] P. Wang, H. Jung, Y. Li, S. Shen, R. P. Srikant, L. Garattoni, S. Meier, N. Navab, and B. Busam, “Phocal: A multi-modal dataset for category-level object pose estimation with photometrically challenging objects,” in *Proceedings of the IEEE/CVF Conference on Computer Vision and Pattern Recognition (CVPR)*, June 2022, pp. 21 222–21 231.
- [28] X. Liu, S. Iwase, and K. M. Kitani, “Stereoobj-1m: Large-scale stereo image dataset for 6d object pose estimation,” in *Proceedings of the IEEE/CVF International Conference on Computer Vision*, 2021, pp. 10 870–10 879.
- [29] H. Wang, S. Sridhar, J. Huang, J. Valentin, S. Song, and L. J. Guibas, “Normalized object coordinate space for category-level 6d object pose and size estimation,” in *The IEEE Conference on Computer Vision and Pattern Recognition (CVPR)*, June 2019.
- [30] M. Tancik, E. Weber, E. Ng, R. Li, B. Yi, T. Wang, A. Kristoffersen, J. Austin, K. Salahi, A. Ahuja *et al.*, “Nerfstudio: A modular framework for neural radiance field development,” in *ACM SIGGRAPH 2023 Conference Proceedings*, 2023, pp. 1–12.
- [31] J. T. Barron, B. Mildenhall, D. Verbin, P. P. Srinivasan, and P. Hedman, “Zip-nerf: Anti-aliased grid-based neural radiance fields,” in *Proceedings of the IEEE/CVF International Conference on Computer Vision*, 2023, pp. 19 697–19 705.
- [32] Z. Yu, A. Chen, B. Huang, T. Sattler, and A. Geiger, “Mip-splatting: Alias-free 3d gaussian splatting,” *arXiv:2311.16493*, 2023.
- [33] R. Zhang, P. Isola, A. A. Efros, E. Shechtman, and O. Wang, “The unreasonable effectiveness of deep features as a perceptual metric,” in *CVPR*, 2018.
- [34] Z. Zhu, S. Peng, V. Larsson, W. Xu, H. Bao, Z. Cui, M. R. Oswald, and M. Pollefeys, “Nice-slam: Neural implicit scalable encoding for slam,” in *Proceedings of the IEEE/CVF Conference on Computer Vision and Pattern Recognition (CVPR)*, 2022.
- [35] H. Wang, J. Wang, and L. Agapito, “Co-slam: Joint coordinate and sparse parametric encodings for neural real-time slam,” in *CVPR*, 2023.
- [36] V. Yugay, Y. Li, T. Gevers, and M. R. Oswald, “Gaussian-slam: Photo-realistic dense slam with gaussian splatting,” 2023.
- [37] J. Sturm, N. Engelhard, F. Endres, W. Burgard, and D. Cremers, “A benchmark for the evaluation of rgb-d slam systems,” in *2012 IEEE/RSJ International Conference on Intelligent Robots and Systems*, Sep 2012. [Online]. Available: <http://dx.doi.org/10.1109/iros.2012.6385773>

- [38] E. Sucar, S. Liu, J. Ortiz, and A. J. Davison, “imap: Implicit mapping and positioning in real-time,” in *Proceedings of the IEEE/CVF International Conference on Computer Vision*, 2021, pp. 6229–6238.
- [39] D. Azinović, R. Martin-Brualla, D. B. Goldman, M. Nießner, and J. Thies, “Neural rgb-d surface reconstruction,” in *Proceedings of the IEEE/CVF Conference on Computer Vision and Pattern Recognition (CVPR)*, June 2022, pp. 6290–6301.
- [40] J. Kim, J. Kim, J. Na, and H. Joo, “Parahome: Parameterizing everyday home activities towards 3d generative modeling of human-object interactions,” *arXiv preprint arXiv:2401.10232*, 2024.

## Checklist

1. For all authors...
  - (a) Do the main claims made in the abstract and introduction accurately reflect the paper’s contributions and scope? [Yes]
  - (b) Did you describe the limitations of your work? [Yes] See Section 6.
  - (c) Did you discuss any potential negative societal impacts of your work? [Yes] See Section 6.
  - (d) Have you read the ethics review guidelines and ensured that your paper conforms to them? [Yes]
2. If you are including theoretical results...
  - (a) Did you state the full set of assumptions of all theoretical results? [N/A]
  - (b) Did you include complete proofs of all theoretical results? [N/A]
3. If you ran experiments (e.g. for benchmarks)...
  - (a) Did you include the code, data, and instructions needed to reproduce the main experimental results (either in the supplemental material or as a URL)? [Yes] Data is released (see footnote in page 2), benchmark results with existing methods provided.
  - (b) Did you specify all the training details (e.g., data splits, hyperparameters, how they were chosen)? [Yes] Data split are provided (See Sec. 5). Hyperparameters are taken from existing SotA.
  - (c) Did you report error bars (e.g., with respect to the random seed after running experiments multiple times)? [No] Following evaluations metrics for provided 3D tasks, we did not.
  - (d) Did you include the total amount of compute and the type of resources used (e.g., type of GPUs, internal cluster, or cloud provider)? [Yes] See Section 5.
4. If you are using existing assets (e.g., code, data, models) or curating/releasing new assets...
  - (a) If your work uses existing assets, did you cite the creators? [Yes]
  - (b) Did you mention the license of the assets? [Yes] See Supplementary Material.
  - (c) Did you include any new assets either in the supplemental material or as a URL? [Yes] Link to download new dataset is provided (see footnote in page 2).
  - (d) Did you discuss whether and how consent was obtained from people whose data you’re using/curating? [N/A]
  - (e) Did you discuss whether the data you are using/curating contains personally identifiable information or offensive content? [N/A] Data does not provide personally identifiable information or offensive content.
5. If you used crowdsourcing or conducted research with human subjects...
  - (a) Did you include the full text of instructions given to participants and screenshots, if applicable? [N/A]
  - (b) Did you describe any potential participant risks, with links to Institutional Review Board (IRB) approvals, if applicable? [N/A]
  - (c) Did you include the estimated hourly wage paid to participants and the total amount spent on participant compensation? [N/A]

---

# Supplementary Material For SCRREAM

---

**HyunJun Jung**

Technical University of Munich  
hyunjun.jung@tum.de

**Weihang Li**

Technical University of Munich

**Shun-Cheng Wu**

Technical University of Munich

**William Bittner**

Technical University of Munich

**Nikolas Brasch**

Technical University of Munich

**Jifei Song**

Huawei Noah's Ark Lab

**Eduardo Pérez-Pellitero**

Huawei Noah's Ark Lab

**Zhensong Zhang**

Huawei Noah's Ark Lab

**Arthur Moreau**

Huawei Noah's Ark Lab

**Nassir Navab**

Technical University of Munich

**Benjamin Busam**

Technical University of Munich  
b.busam@tum.de

## 1 Hardware Setup

We use a specially designed camera rig (Fig. 1, (a)) to capture the synchronized multi-modal image sequences in a free hand manner. RGB and polarization images are acquired with a Phoenix 5.0 MP Polarization camera (PHX050S1-QC, LUCID Vision Labs, Canada) equipped with a Sony Polarsens sensor (IMX264MYR CMOS, Sony, Japan). For the depth images, we use two depth modality, active stereo depth and indirect time-of-flight depth. Intel RealSense D435 (Intel, USA) is used for the active stereo depth and Lucid Helios (HLS003S-001, LUCID Vision Labs, Canada) is used for indirect time-of-flight depth. For synchronization, a Raspberry Pi generates a trigger signal that is connected to all cameras to trigger the image acquisition.

Two different types of scanners are used for the scanning. For the small household objects, such as cups or water bottles, we use the table-top scanner (EinScan-SP, SHINING 3D Tech. Co., Ltd., Hangzhou, China, Fig. 1, (b)) to capture the meshes with fine details. For the larger objects that do not fit to the table-top scanner, such as furniture or medium size objects or room, we use hand held scanner (Artec-Leo, Artec 3D, Luxembourg, Fig. 1, (c)) that runs SLAM internally for tracking the scanning. To scan large texture-less areas, such as walls or big tables, we use small stripes of masking tape on the surface to provide additional texture (Fig. 2, (a)) during the scanning. Later, the textures from the masking tapes are removed via the texture healing function in Artec Studio 17 ((Fig. 2, (b)).

## 2 Dataset Examples

**Indoor Reconstruction and SLAM Dataset.** We provide 11 scenes that comprise 7114 frames, 94 object & furniture meshes and 7 indoor room meshes for the indoor reconstruction and SLAM dataset. Note that all furniture and objects in the scenes are scanned prior to ensure the meshes are high resolution and water-tight, in order to serve as digital twin assets so that the rendered depth does not miss any parts of the scene. The visualization of each scene mesh is shown in Fig. 3.

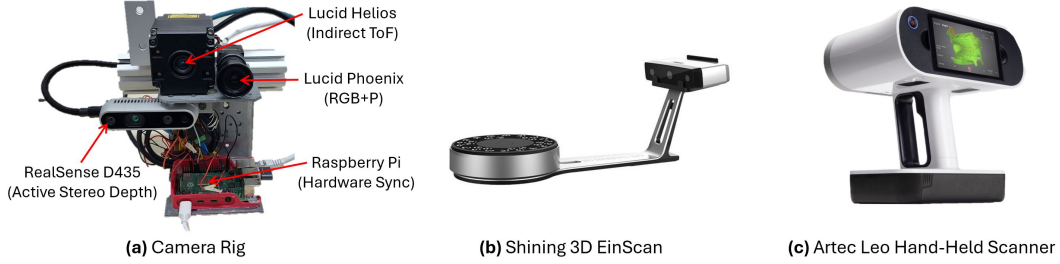


Figure 1: **Hardware Setup.**

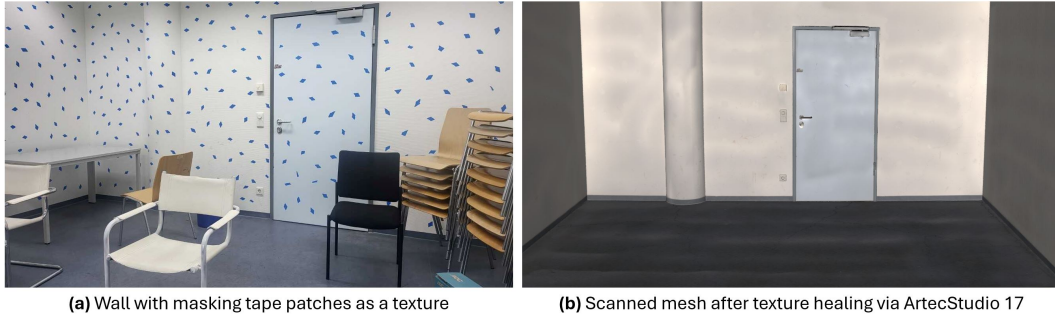


Figure 2: **Example of Wall Scanning.** To help tracking the hand-held scanner on the plain white wall, we attach patches of masking tape on the wall to provide additional texture (a). Later, the texture of the tape can be removed in a post-processing step (b).

**Object Removal & Scene Editing Dataset.** We capture multiple additional video sequences for each of the 8 selected scenes from the indoor reconstruction and SLAM dataset each with a reduced number of objects or furniture to obtain multiple examples for object removal and scene editing tasks. This set is comprised of additional 9323 frames. A visualization of each reduced scene is shown in Fig. 4- 11. Note that for each reduced scene, we capture the real image sequence with the camera rig.

**Human Reconstruction Dataset.** For the semi-dynamic human sequences with the mannequin, we do scanning, registration, rendering and mapping for all individual frames. We showcase 2 scenes captured with this setup. We show the scene with a single human mesh from the first frame (Fig 12, left) to show the scene setup as well as all human meshes from the entire video sequence (Fig 12, right) to show the motion range of the mannequin. Note that around 4 real images are captured per time frame for the mapping step.

**6D Pose Estimation Dataset.** We showcase two pose dataset scenes in Fig 13. By nature of our dataset annotation pipeline, we can obtain object poses w.r.t. the world coordinate system  $T_{obj \rightarrow world}$  and camera poses w.r.t. the world coordinate system  $T_{cam \rightarrow world}$ . By concatenating both pose in the right order (e.g.  $T_{obj \rightarrow world}^{-1} \cdot T_{obj \rightarrow world}$ ), the object pose w.r.t. the camera center  $T_{obj \rightarrow cam}$ , the so called 6D object pose, can be obtained. Having registered the object poses using our framework, the free-hand camera rig can be used to quickly and easily capture a pose dataset with extensive camera coverage.



Figure 3: Example of Indoor Reconstruction and SLAM Scenes.



Figure 4: Example of Reduced Scenes For Scene01.

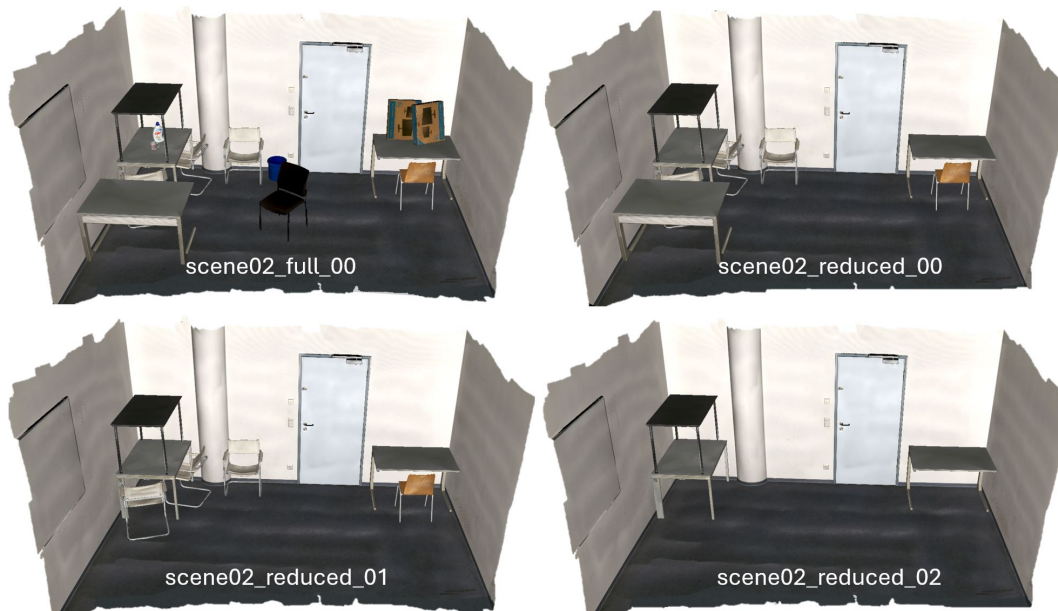


Figure 5: Example of Reduced Scenes For Scene02.

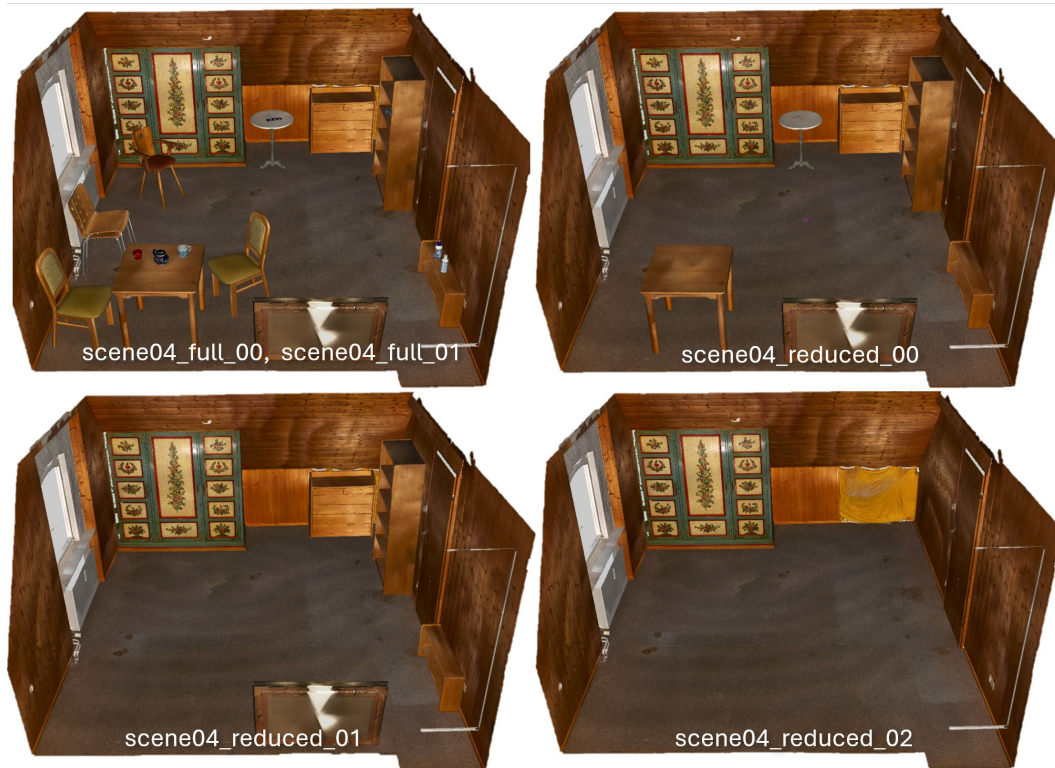


Figure 6: Example of Reduced Scenes For Scene04.



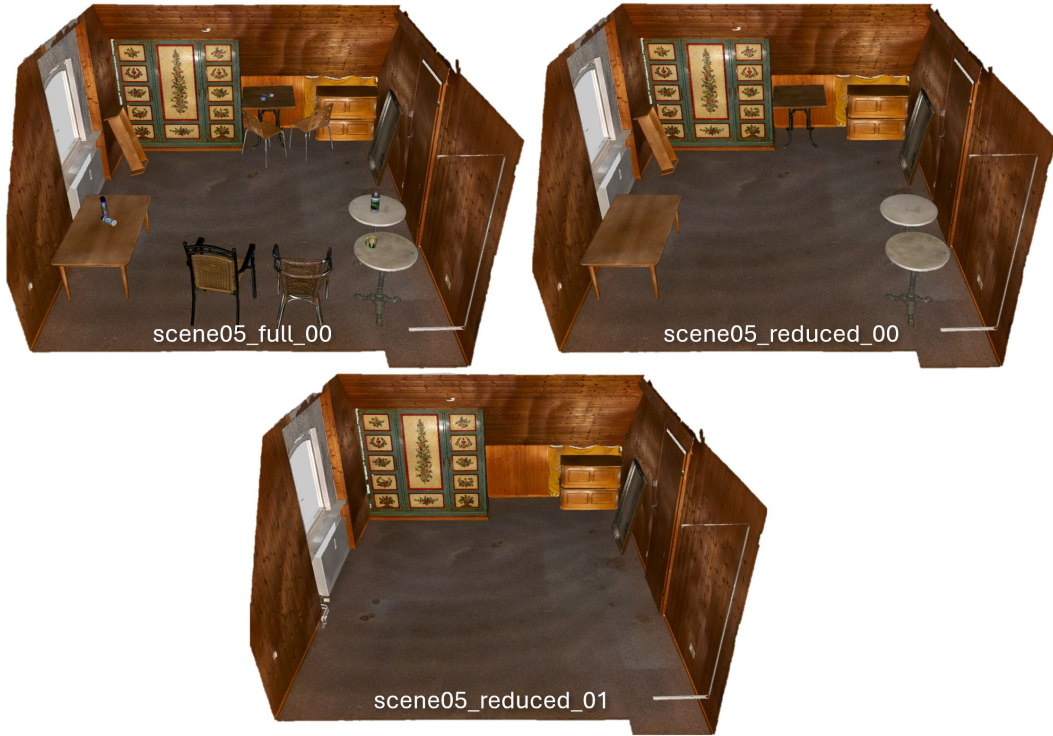


Figure 7: Example of Reduced Scenes For Scene05.



Figure 8: Example of Reduced Scenes For Scene06.

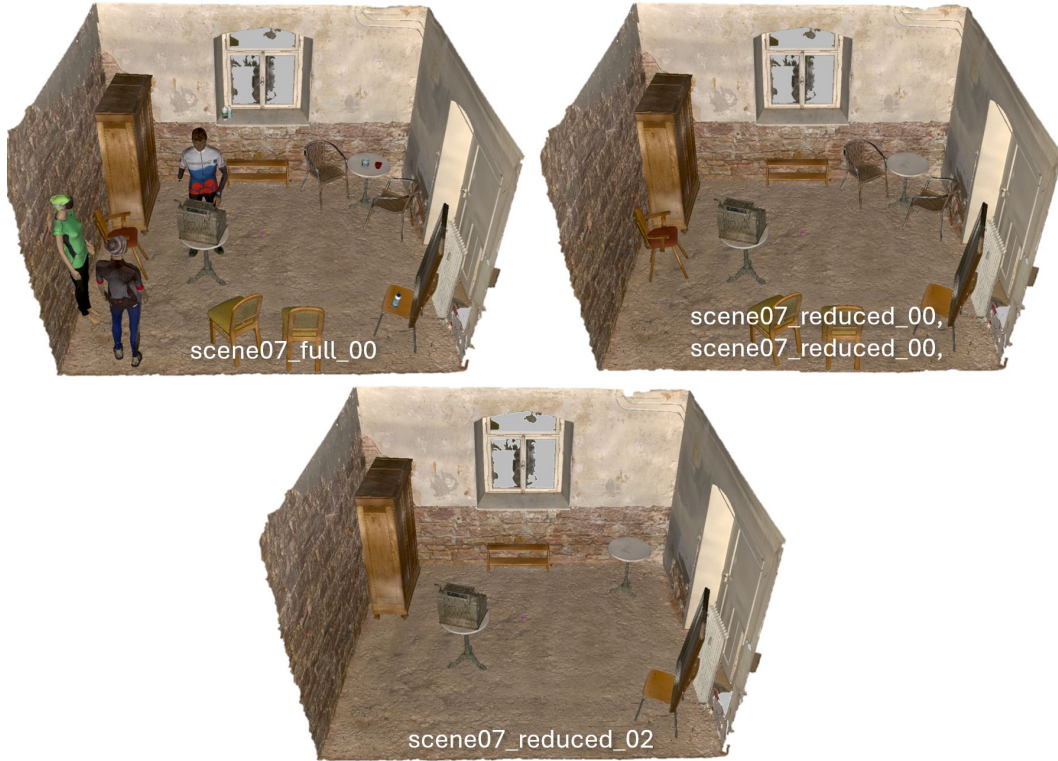


Figure 9: Example of Reduced Scenes For Scene07.

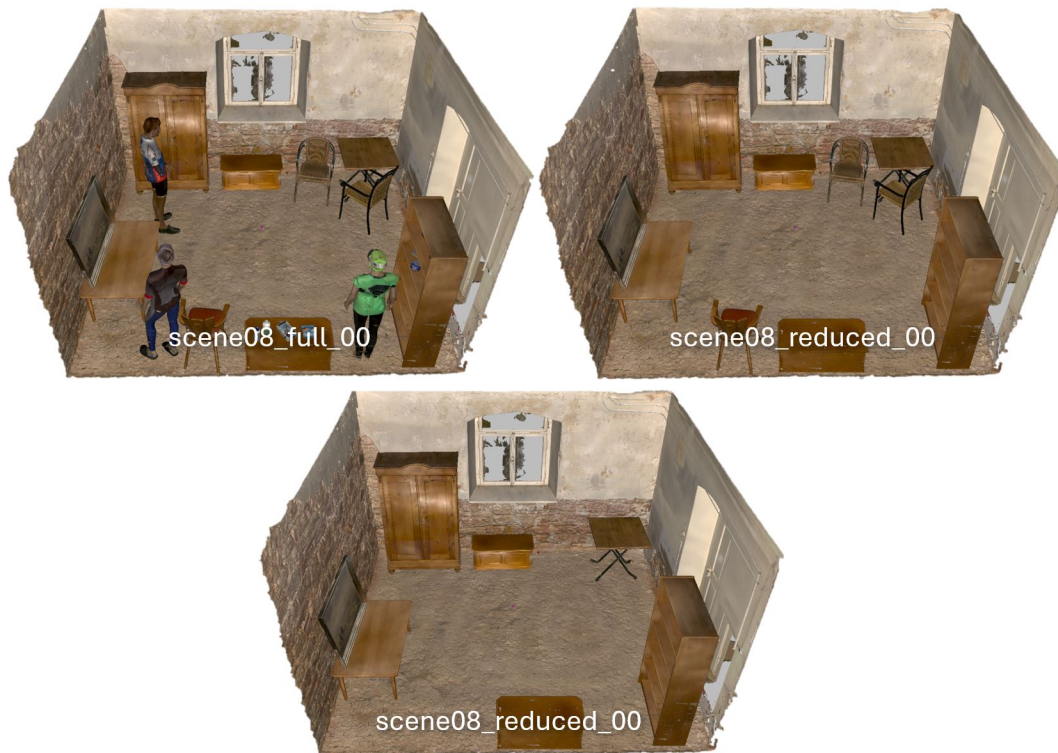


Figure 10: Example of Reduced Scenes For Scene08.

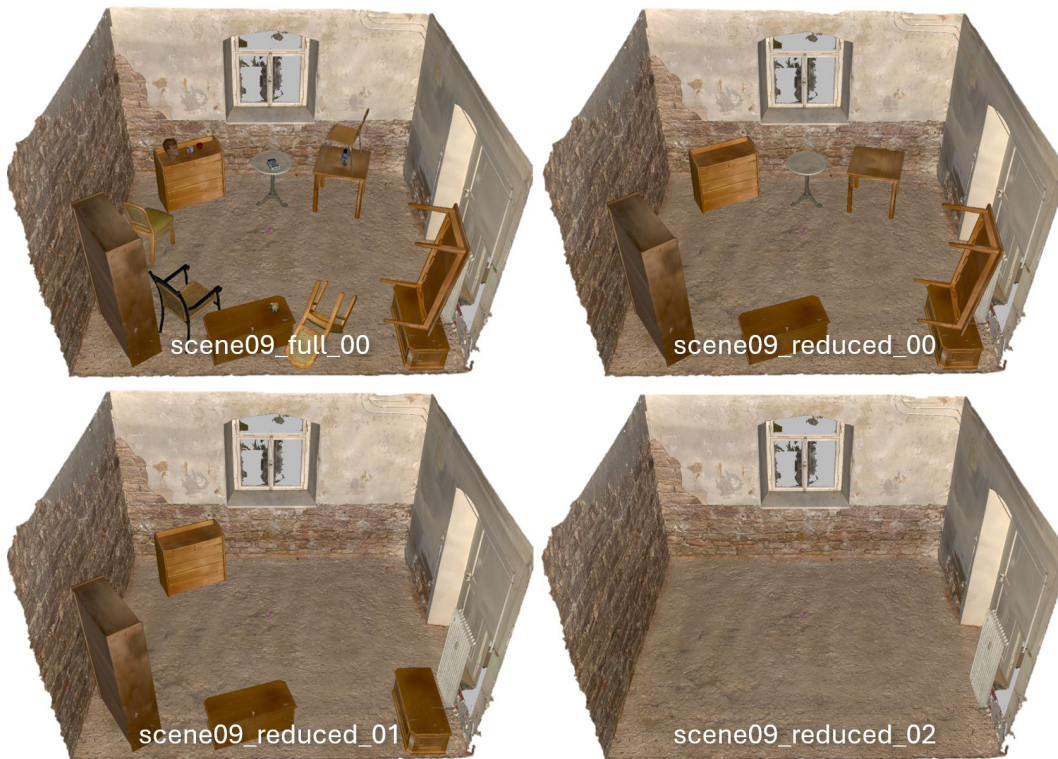


Figure 11: Example of Reduced Scenes For Scene09.

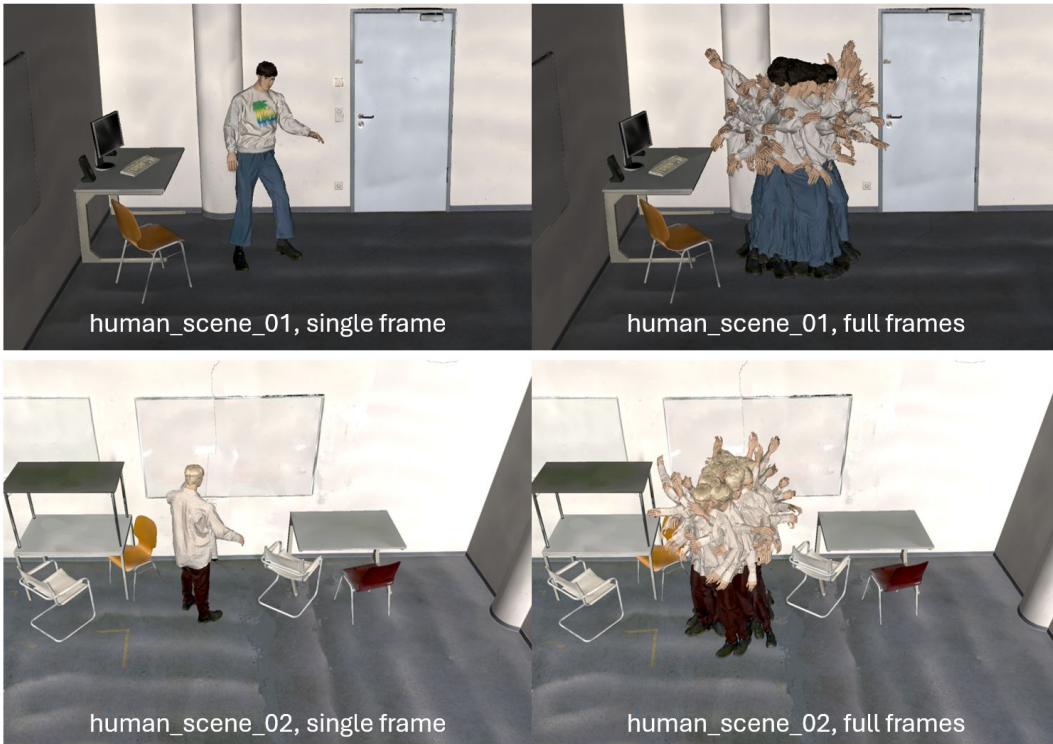


Figure 12: Example of Human Dataset Scenes.



Figure 13: Example of Pose Dataset Scenes.

### 3 Dataset Comparison

In this section, we show more in-depth comparisons between the existing indoor datasets and our dataset using meshes of the scanned scenes. We choose the ScanNet++ [7] and Replica dataset [6] for comparison.

The ScanNet++ dataset is an improved version of ScanNet [3]. Instead of using a commercial depth sensor like its predecessor, ScanNet++ uses a LiDAR sensor that rotates and captures a more accurate 360° pointcloud of the scene. To be less dependent on the sensor’s line-of-sight ScanNet++ captures the scene from multiple locations in the scene in order to improve the quality and completeness of the mesh. However, no post-processing is applied, such as hole filling, so that the final mesh still has many missing parts, limiting the use of the scene meshes as ground truth for rendering complete views. This is because for the areas with missing geometry the background is visible instead of the foreground such that a metric using the incomplete mesh as ground truth will penalize a method that models the foreground object correctly. We show in Fig. 14 that our dataset provides the full details on the office furniture such as the chairs, the trash bin, the monitor etc while ScanNet++ suffers from incomplete and missing parts in the mesh.

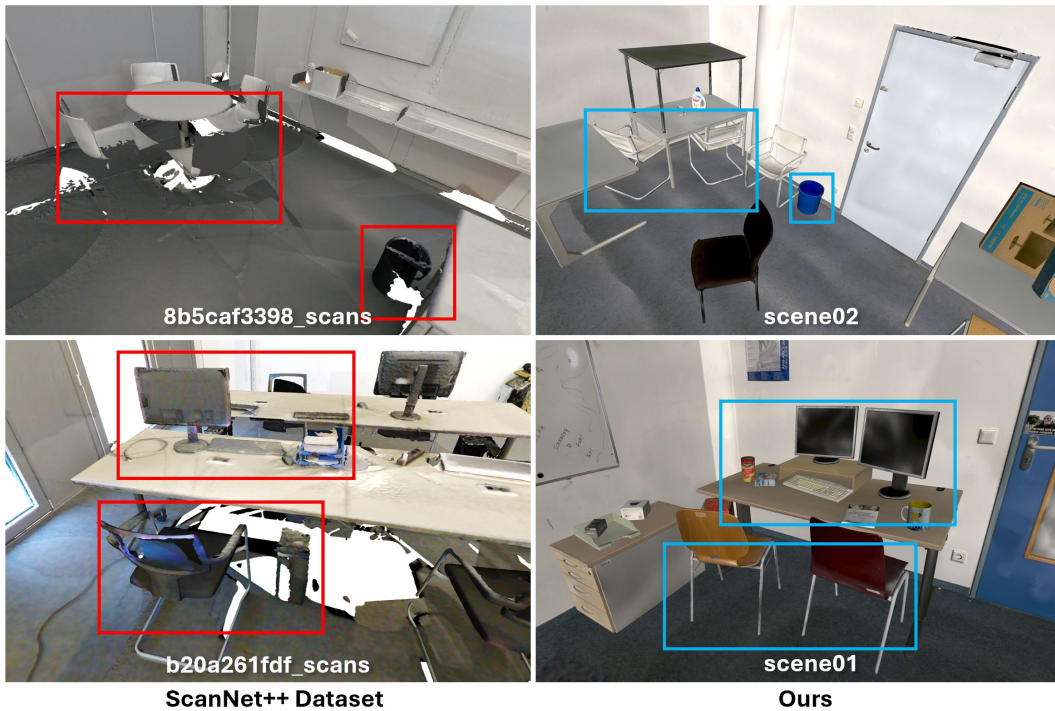


Figure 14: ScanNet++ Dataset VS Ours.

Unlike ScanNet++, the Replica dataset scans the scene with a specially designed camera rig that contains multiple sensors to obtain the mesh in more detail. Also, after the scanning, a manual hole-filling process is used to complete the mesh if the missing area is part of a flat surface. For this reason, the meshes of the Replica dataset are much more complete compared to ScanNet++. However, we find that meshes in the Replica dataset in general are overly smoothed and lack details. Also there are parts missing on non-flat surfaces, such as the legs of a chair or the tab of the sink. In Fig. 15 we provide a comparison between the Replica dataset and our dataset. We show a kitchen scene from each dataset to demonstrate that compared with Replica our dataset contains all small details of the scene, such as the small handles of the kitchen cabinet (zoom in for more details). We also show that the legs of the chairs and table are missing in a living room scene from the Replica dataset, while our dataset contains these parts in a high quality.

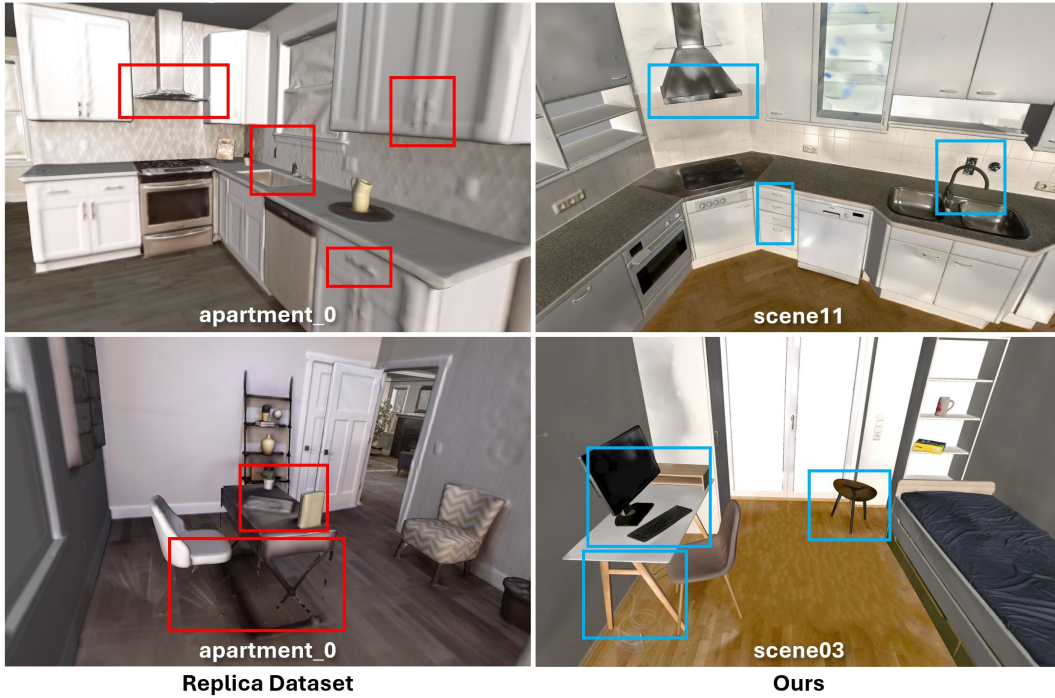


Figure 15: **Replica Dataset VS Ours.**

## 4 Dataset Documentation

Our dataset includes scene folders with 3 different conventions. Folders with the "sceneXX" convention contain data for the Indoor Reconstruction and SLAM Dataset and Object Removal and Scene Editing Dataset, folders with labelled "human\_sceneXX" contain the Human Reconstruction Dataset and folders named "pose\_sceneXX" contain the 6D Pose Estimation Dataset. In this section, we explain the file structure of the dataset and describe the naming conventions for individual files in the folders. To access the dataset's download link as well as python code for data loading and visualization, please visit <https://github.com/Junggy/SCRREAM>.

### 4.1 Indoor Reconstruction and SLAM Dataset and Object Removal and Scene Editing Dataset.

Both the Indoor Reconstruction and SLAM Dataset and the Object Removal and Scene Editing Dataset follow the same format. The "sceneXX" folders contain 3 sub-folders: "meshes", "sceneXX\_full\_XX" and "sceneXX\_reduced\_XX".

The "meshes" folder contains independent meshes of the full scene that are aligned w.r.t. world coordinate system as "\*.obj" files. Therefore loading all meshes together shows the full scene in the world coordinate system. Each mesh file follows a naming convention of "{class\_name}-{instance\_name}.obj". For example, a monitor object with of the old\_tall instance is named "monitor-old\_tall.obj". This naming convention allows easy identification of both class and instance of the objects in the scene.

The "sceneXX\_full\_XX" and "sceneXX\_reduced\_XX" folders contain the data regarding the image sequences, such as "camera\_pose", "depth\_d435", "depth\_gt", "depth\_tof", "instance", "pol", "rgb", "sparse", "intrinsic.txt", "meta.txt" and "video.avi". The detailed folder layout is shown in Fig. 16. Both full scene and reduced scene have the same file structure. Metadata from "meta.txt" can be used to identify the removed objects in the reduced scenes.

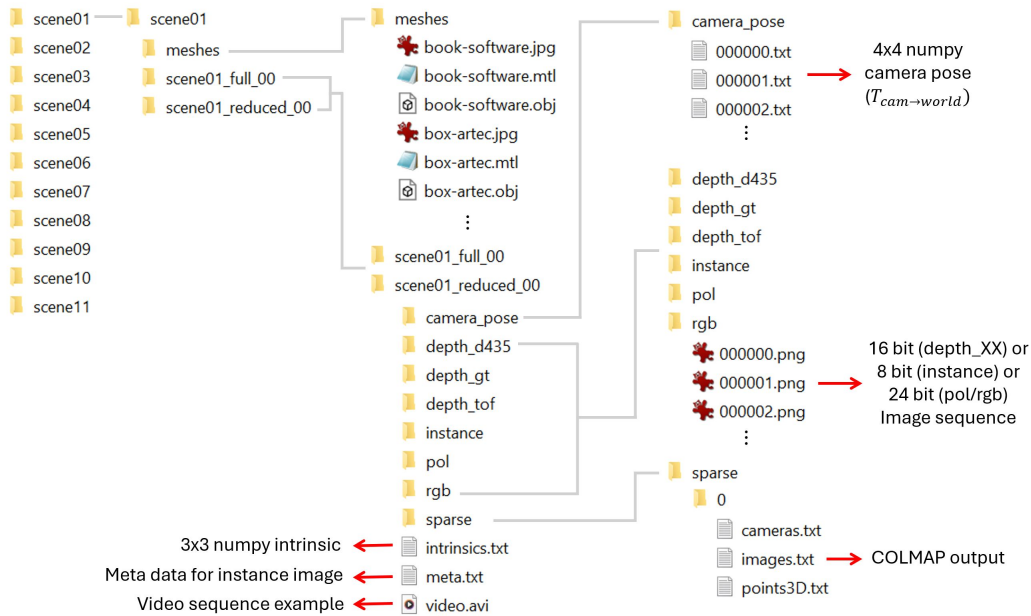


Figure 16: File Structure of the Indoor Reconstruction and SLAM Dataset and Object Removal and Scene Editing Dataset.

The "camera\_pose" folder contains the camera pose for each image frame in the 4x4 matrix format saved as numpy matrix in a text file. The camera pose's definition is  $T_{cam \rightarrow world}$ , meaning that each frame's translation element refers to the camera center in the scene. The matrix can be loaded with the "np.loadtxt" function.

The "depth\_d435", "depth\_gt", "depth\_tof" folders contain the depth images for each image frame. Each depth image is saved as a 16bit image in *mm* units meaning that pixel value 1000 represents 1 meter. The depth images can be loaded in meter units by using opencv-python's "cv2.imread" function, "cv2.imread("XXXXXX.png", -1).astype(np.uint16)/1000". Images from both the "depth\_d435" and "depth\_tof" folders are obtained from the real depth sensors and warped or aligned to the RGB image in a forward manner (e.g. forward-warping) using their own depth values, the extrinsic calibration matrix and RGB sensor's intrinsic matrix. Note that due to sensor noise, the warped depth are often not well aligned to the corresponding RGB image. Images in the "depth\_gt" folder are the ground truth depth maps that are rendered from the object meshes and camera poses and serve as absolute ground truth for the depth evaluation benchmark.

The "instance" folder contains the corresponding instance segmentation images for the given RGB frames. The segmentation is obtained by rendering the individual objects with a unique value using the camera pose and intrinsic matrix. The mapping between the pixel values and object instances is provided in the "meta.txt" file. We keep the same mapping between the full and reduced scenes for convenience.

The "meta.txt" file contains the metadata that is mapping between the instance pixel values and the object meshes in the scene. Each line of metadata follows the convention of "{class\_name}{mesh\_name} {pixel\_value}". For example if the pixel value of "keyboard-grey\_old" is 165 in the instance image, its written as "keyboard keyboard-grey\_old 165". With this, one can convert the instance segmentation image into a class segmentation image. Note that this metadata shares the same mapping value per scene, for example "room room-office 240" is in the metadata from both "scene01\_full\_00" and "scene01\_reduced\_00", while as "keyboard-grey\_old" is not present in "scene01\_reduced\_00", the metadata does not contain "keyboard keyboard-grey\_old 165" (Fig. 17).



Figure 17: Example of Instance Segmentation and Metadata Mapping for a Full and Reduced Scene.

The "pol" folder contains polarimetric images obtained from the Lucid Phoenix polarization camera. Polarimetric images are stored as 4 RGB images with 4 different polarization angles (0,45,90,135 degree) arranged in a clockwise manner starting from the left top side. All 4 images are un-distorted so that no distortion coefficient is needed and intrinsic matrix is saved in "intrinsics.txt".

The "rgb" folder contains the RGB image sequence. The RGB images are obtained by averaging the 4 polarization images and share the same intrinsics as "intrinsics.txt".

The "sparse" folder contains the COLMAP [18, 19] output that is obtained by running COLMAP with the ground truth camera pose. We fix the camera poses to keep the scale unchanged. We specifically provide this folder to make our dataset compatible with 3D Gaussian Splatting [13] variants.

The "video.avi" is an example video that serves as qualitative evaluation of the camera trajectory as well as annotation quality. The video contains the visualization of depth maps and depth error and the instance image overlaid on the RGB image as shown in Fig. 18.



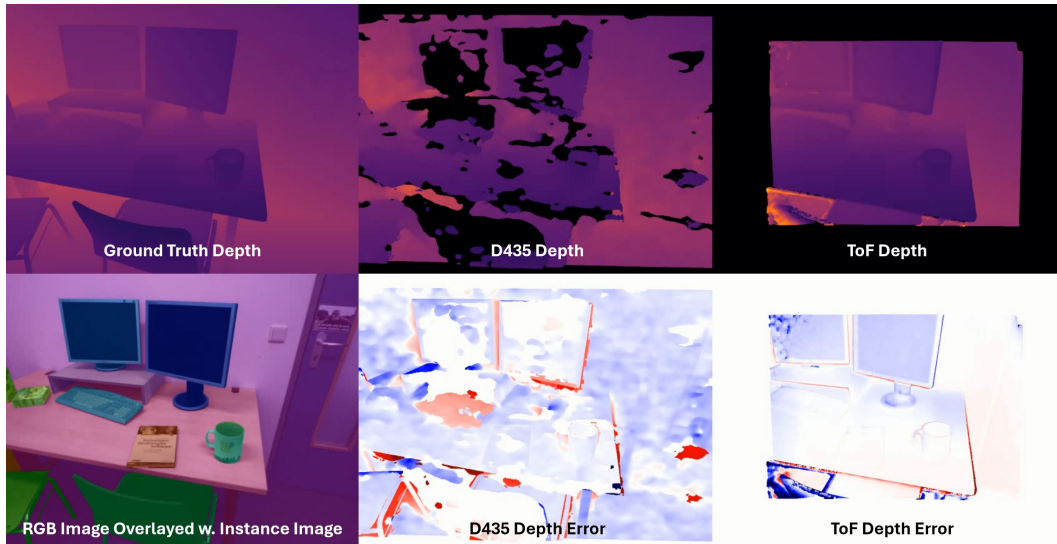


Figure 18: **Example of the video.avi layout.**

## 4.2 Human Reconstruction Dataset

The Human Reconstruction Dataset shares a similar file structure as the Indoor Reconstruction and SLAM Dataset and the Object Removal and Scene Editing Dataset. There are a few differences in the folder arrangement as well as file naming convention as 4 images are captured per human posture. See Fig. 19 for an overview.

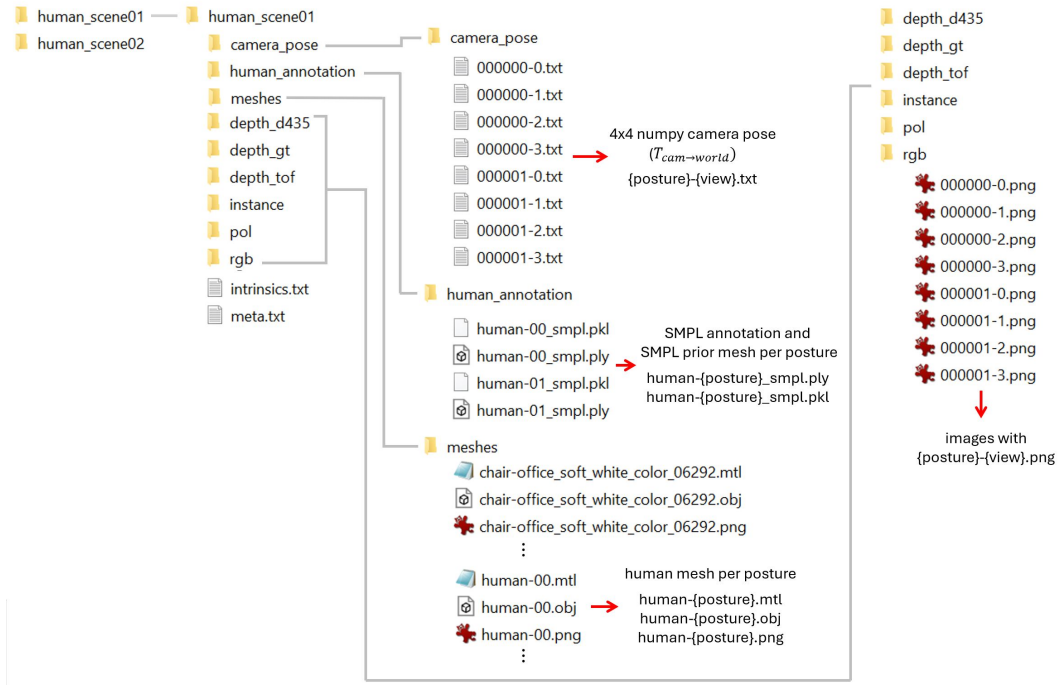


Figure 19: **File Structure of the Human Reconstruction Dataset.**

The "meshes" folder contains the meshes of the scene as in the previous dataset setup. However, the folder contains all human meshes from different postures as well. We capture 45 postures for "human\_scene\_01" and 37 postures for "human\_scene\_02". Each human posture is scanned with the hand-held scanner in a high resolution and water-tight manner like the other objects meshes and we save the mesh with the naming convention "human-`{posture}`.obj".

The "human\_annotation" folder contains SMPL [24] parameter annotations for each human posture. The \*.pkl" files contain SMPL annotations as a python pickle file and the \*.ply" files are the SMPL vertices / mesh generated from the pickle file. Both files follow the convention of "human-`{posture}`\_smpl" with extension of \*.pkl" and \*.ply". The \*.pkl"s SMPL annotation follows the same convention as in [25, 26] that contains a 72 channel vector for the "pose" (first 3 channels are for "global\_orient", the remaining 69 channels are for the "body\_pose"), a 300 channel vector for the shape "betas" and a 3 channel vector for the translation "trans".

The "camera\_pose" folder contains the camera pose for each image frame in the 4x4 matrix format as in the reconstruction and SLAM dataset. However, as the human dataset captures 4 multi-view images on single human posture, it contains 4 poses per posture. Camera poses files are saved with the convention "`{posture}`-`{view}`.txt".

All image files including depths, RGBs, instances are saved the same way as in the Reconstruction and SLAM dataset but saved with the same convention as for the camera poses due to the 4 multi-view images captured per human posture. All images follow the same convention of "`{posture}`-`{view}`.png".

While "meta.txt" has the same mapping information as in the previous dataset setup, plus the humans with the convention of "human 00 `{pixel_value}`". For the humans no mesh name is provided in the middle as there are multiple human meshes per scene but all share the same pixel value in the instance images throughout the same scene.

### 4.3 6D Pose Estimation Dataset

The contents in the "6D Pose Estimation Dataset" share the same principle as in the Indoor Reconstruction and SLAM Dataset and Object Removal and Scene Editing Dataset for the image folders ("depth\_d435", "depth\_gt", "depth\_tof", "depth\_instance", "pol", "rgb"), "intrinsic.txt" and "meta.txt" files, while it contains additional folders, such as "pose\_meshes\_canonical" and "labels" for the 6D pose annotation. An overview of the file structure is shown in Fig. 20.

The "pose\_meshes\_canonical" folder contains the meshes of the target objects for the pose estimation in canonical orientation in contrast to the meshes in "meshes" in the other dataset format that are defined in world coordinates. The canonical meshes are self-centered (object center is in the center of its bounding box) and follow specific orientation convention per class or category (Fig. 21, (a)), while the meshes from the previous dataset are centered and oriented according to their layout in the scene (Fig. 21, (b)). Although they have differences in their orientation, we follow the same naming convention as "`{class_name}`-`{instance_name}`.obj".

The "labels" folder contains the 6D pose annotation information as a pickle file with the convention of "`{frame}_label.pkl`". We provide the pickle file in a similar format as the NOCS [29] dataset's labels. Each pickle file contains a python dictionary of the following keys: "model\_list", "instance\_ids", "class\_ids", "scales", "rotations", "translations", "bboxes", "gt\_scales".

1. "model\_list" is a python list containing a tuple of each object's name and pixel value in the instance image, such as [{"obj\_1\_name"}, {instance\_value\_1}], [{"obj\_2\_name"}, {instance\_value\_2}] ... ].
2. "instance\_ids" is a python list containing the instance value per object in the same order as "model\_list", such as [{instance\_value\_1}, {instance\_value\_2}] ... ].
3. "class\_ids" is a python list containing the mapping between the class name and a predefined class id in the same order, such as [{class\_id\_1}, {class\_id\_2}] ... ].
4. "scales" is a python list containing the diagonal length of each object in the same order, such as [{diag\_length\_1}, {diag\_length\_2}] ... ].

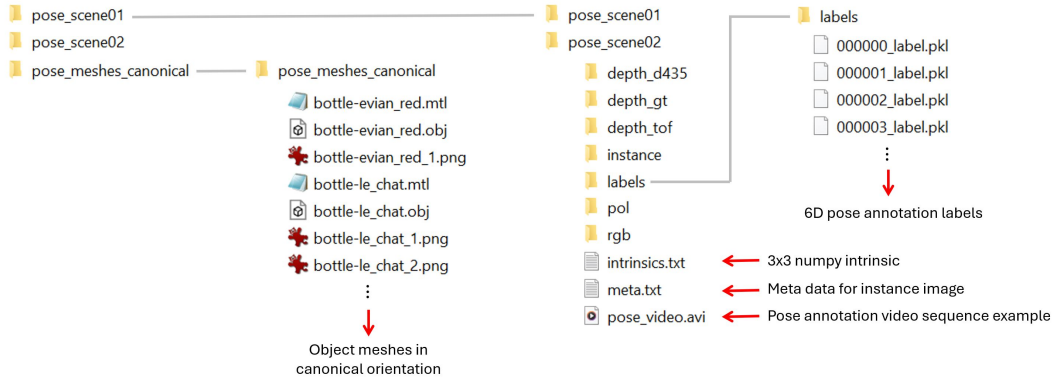


Figure 20: File Structure of the 6D Pose Estimation Dataset.

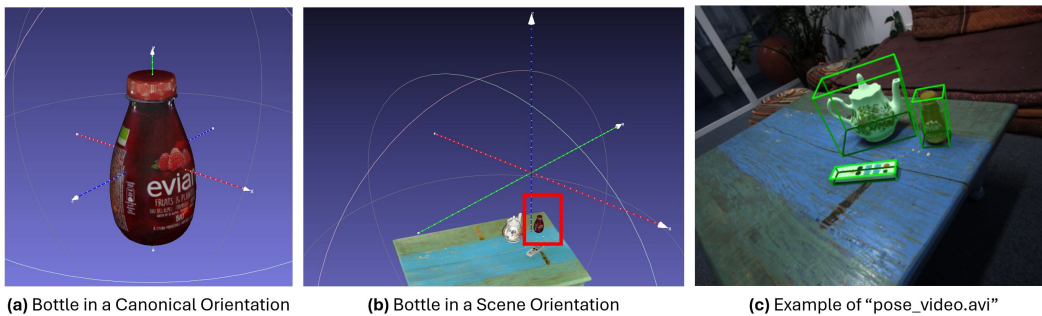


Figure 21: **Example of Meshes and "pose\_video.avi"**. The object in the canonical orientation is self centered and oriented according to a specific convention (i.e. standing with y-axis), while the object in the scene orientation is oriented according to the scene's layout. The meshes are visualized in Meshlab [? ].

5. "rotation" is a numpy array of shape  $(n\_objects, 3, 3)$  that is an array of rotation matrices for each object stacked along the first dimension in the same order.
6. "translation" is a numpy array of shape  $(n\_objects, 3)$  that is an array of translation vectors for each object stacked along the first dimension in the same order.
7. "bboxes" is a numpy array of shape  $(n\_objects, 4)$  that is an array of 2D bounding box annotations in the format  $[\{top\_left\_y\}, \{top\_left\_x\}, \{bottom\_right\_y\}, \{bottom\_right\_x\}]$  stacked along the first dimension in the same order.
8. "gt\_scales" is a numpy array of shape  $(n\_objects, 3)$  that is an array with the mesh size in the format  $[\{size\_x\}, \{size\_y\}, \{size\_z\}]$  stacked along the first dimension in the same order.

The "pose\_video.avi" file contains the visualization of the pose annotation as 3D bounding boxes and rendered object masks on the RGB video for a qualitative evaluation of the pose annotation accuracy as well as camera trajectory coverage (Fig. 21).

## 5 Full Benchmarks

In this section, we show the benchmark results of NVS and SLAM for each scene separately.

### 5.1 Novel View Synthesis

In this study, the poor performance of NeRFacto [30] in both RGB and depth quality demonstrates the limitations in the model’s ability to learn fine details and accurate geometry. In contrast, Gaussian-Splatting [13], Mip-Splatting [32], and Zip-NeRF [31] demonstrate superior performance in RGB image reconstruction. These methods prioritize visual fidelity, resulting in high-quality image outputs. However, the lack of geometric constraints in these models means that while they excel in producing visually appealing images, they fall short in accurately capturing and reconstructing depth information. Focusing on depth estimation, Depth-Facto [30] (AS) and Depth-Facto [30] (ToF) stand out for their exemplary performance in depth estimation metrics. These methods leverage the integration of multi-modal sensor data, which acts as an additional constraint, enhancing their ability to accurately predict depth. The utilization of both AS and ToF sensor data demonstrates the significant advantage of incorporating diverse and complementary data sources, leading to improved depth estimation performance.

Table 1: NVS Benchmark for scene01

Evaluation	RGB			Depth					
	Method	PSNR $\uparrow$	SSIM $\uparrow$	LPIPS $\downarrow$	RSME $\downarrow$	Abs Rel $\downarrow$	Sqr Rel $\downarrow$	<1.25 <sup>1</sup> $\uparrow$	<1.25 <sup>2</sup> $\uparrow$
NeRFacto [30]	22.346	0.801	0.258	0.814	0.414	0.529	0.564	0.728	0.807
Depth-Facto [30] (AS)	25.313	0.828	0.244	0.224	0.086	0.068	0.939	0.956	0.964
Depth-Facto [30] (ToF)	25.267	0.827	0.242	0.300	0.090	0.099	0.908	0.928	0.941
Zip-NeRF [31]	29.548	0.832	0.142	0.322	0.177	0.075	0.647	0.955	0.972
Gaussian-Splatting [13]	28.282	0.848	0.279	0.322	0.133	0.068	0.777	0.904	0.952
Mip-Splatting [32]	28.384	0.848	0.278	0.309	0.122	0.061	0.803	0.925	0.956

Table 2: NVS Benchmark for scene02

Evaluation	RGB			Depth					
	Method	PSNR $\uparrow$	SSIM $\uparrow$	LPIPS $\downarrow$	RSME $\downarrow$	Abs Rel $\downarrow$	Sqr Rel $\downarrow$	<1.25 <sup>1</sup> $\uparrow$	<1.25 <sup>2</sup> $\uparrow$
NeRFacto [30]	24.011	0.808	0.300	1.243	0.528	0.951	0.493	0.635	0.763
Depth-Facto [30] (AS)	26.062	0.835	0.283	0.228	0.092	0.027	0.981	0.995	0.999
Depth-Facto [30] (ToF)	26.251	0.838	0.275	0.739	0.192	0.372	0.855	0.870	0.898
Zip-NeRF [31]	32.278	0.812	0.190	0.374	0.173	0.074	0.640	0.941	0.994
Gaussian-Splatting [13]	29.616	0.842	0.322	0.483	0.195	0.144	0.683	0.852	0.899
Mip-Splatting [32]	29.230	0.842	0.323	0.531	0.218	0.164	0.610	0.824	0.884

Table 3: NVS Benchmark for scene03

Evaluation	RGB			Depth					
	Method	PSNR $\uparrow$	SSIM $\uparrow$	LPIPS $\downarrow$	RSME $\downarrow$	Abs Rel $\downarrow$	Sqr Rel $\downarrow$	<1.25 <sup>1</sup> $\uparrow$	<1.25 <sup>2</sup> $\uparrow$
NeRFacto [30]	20.823	0.808	0.277	2.093	1.482	3.664	0.129	0.224	0.312
Depth-Facto [30] (AS)	24.227	0.869	0.207	0.500	0.199	0.341	0.915	0.939	0.956
Depth-Facto [30] (ToF)	24.524	0.875	0.236	0.960	0.366	0.816	0.777	0.805	0.827
Zip-NeRF [31]	33.581	0.905	0.117	0.368	0.187	0.086	0.616	0.910	0.969
Gaussian-Splatting [13]	28.928	0.920	0.274	0.531	0.253	0.173	0.452	0.788	0.902
Mip-Splatting [32]	29.304	0.920	0.273	0.527	0.257	0.170	0.444	0.760	0.903

Table 4: NVS Benchmark for scene04, sequence00

Evaluation	RGB			Depth					
	PSNR $\uparrow$	SSIM $\uparrow$	LPIPS $\downarrow$	RSME $\downarrow$	Abs Rel $\downarrow$	Sqr Rel $\downarrow$	<1.25 <sup>1</sup> $\uparrow$	<1.25 <sup>2</sup> $\uparrow$	<1.25 <sup>3</sup> $\uparrow$
NeRFacto [30]	21.880	0.775	0.284	1.102	0.485	0.740	0.431	0.655	0.815
Depth-Facto [30] (AS)	22.803	0.791	0.247	0.262	0.088	0.036	0.950	0.979	0.993
Depth-Facto [30] (ToF)	23.060	0.800	0.246	0.306	0.062	0.055	0.932	0.958	0.977
Zip-NeRF [31]	24.267	0.783	0.232	0.602	0.244	0.208	0.510	0.825	0.914
Gaussian-Splatting [13]	20.037	0.758	0.379	1.002	0.393	0.494	0.321	0.519	0.653
Mip-Splatting [32]	20.605	0.766	0.370	1.032	0.412	0.508	0.271	0.485	0.615

Table 5: NVS Benchmark for scene04, sequence01

Evaluation	RGB			Depth					
	PSNR $\uparrow$	SSIM $\uparrow$	LPIPS $\downarrow$	RSME $\downarrow$	Abs Rel $\downarrow$	Sqr Rel $\downarrow$	<1.25 <sup>1</sup> $\uparrow$	<1.25 <sup>2</sup> $\uparrow$	<1.25 <sup>3</sup> $\uparrow$
NeRFacto [30]	23.323	0.771	0.324	1.216	0.723	1.089	0.269	0.428	0.662
Depth-Facto [30] (AS)	25.453	0.803	0.292	0.268	0.084	0.062	0.951	0.962	0.982
Depth-Facto [30] (ToF)	25.370	0.804	0.288	0.284	0.067	0.069	0.933	0.949	0.967
Zip-NeRF [31]	25.046	0.765	0.344	0.781	0.441	0.498	0.352	0.546	0.610
Gaussian-Splatting [13]	23.207	0.784	0.374	0.691	0.340	0.303	0.374	0.589	0.714
Mip-Splatting [32]	23.008	0.782	0.378	0.711	0.359	0.327	0.356	0.559	0.676

Table 6: NVS Benchmark for scene05

Evaluation	RGB			Depth					
	PSNR $\uparrow$	SSIM $\uparrow$	LPIPS $\downarrow$	RSME $\downarrow$	Abs Rel $\downarrow$	Sqr Rel $\downarrow$	<1.25 <sup>1</sup> $\uparrow$	<1.25 <sup>2</sup> $\uparrow$	<1.25 <sup>3</sup> $\uparrow$
NeRFacto [30]	20.897	0.755	0.371	1.175	0.672	1.025	0.340	0.500	0.688
Depth-Facto [30] (AS)	23.172	0.786	0.360	0.141	0.059	0.016	0.975	0.984	0.993
Depth-Facto [30] (ToF)	23.038	0.785	0.357	0.202	0.058	0.057	0.941	0.960	0.971
Zip-NeRF [31]	24.206	0.770	0.364	0.633	0.348	0.325	0.410	0.654	0.735
Gaussian-Splatting [13]	25.627	0.817	0.345	0.482	0.224	0.160	0.590	0.791	0.879
Mip-Splatting [32]	25.177	0.814	0.345	0.472	0.222	0.158	0.604	0.801	0.880

Table 7: NVS Benchmark for scene06

Evaluation	RGB			Depth					
	PSNR $\uparrow$	SSIM $\uparrow$	LPIPS $\downarrow$	RSME $\downarrow$	Abs Rel $\downarrow$	Sqr Rel $\downarrow$	<1.25 <sup>1</sup> $\uparrow$	<1.25 <sup>2</sup> $\uparrow$	<1.25 <sup>3</sup> $\uparrow$
NeRFacto [30]	23.050	0.809	0.262	0.921	0.420	0.663	0.599	0.789	0.864
Depth-Facto [30] (AS)	24.118	0.813	0.269	0.126	0.035	0.008	0.988	0.997	0.999
Depth-Facto [30] (ToF)	24.106	0.812	0.267	0.098	0.019	0.008	0.988	0.994	0.997
Zip-NeRF [31]	26.724	0.818	0.224	0.403	0.203	0.116	0.623	0.890	0.937
Gaussian-Splatting [13]	26.992	0.833	0.269	0.386	0.141	0.081	0.793	0.948	0.979
Mip-Splatting [32]	26.992	0.833	0.269	0.386	0.141	0.081	0.793	0.948	0.979

Table 8: NVS Benchmark for scene07

Evaluation	RGB			Depth					
	PSNR $\uparrow$	SSIM $\uparrow$	LPIPS $\downarrow$	RSME $\downarrow$	Abs Rel $\downarrow$	Sqr Rel $\downarrow$	<1.25 <sup>1</sup> $\uparrow$	<1.25 <sup>2</sup> $\uparrow$	<1.25 <sup>3</sup> $\uparrow$
NeRFacto [30]	22.820	0.672	0.528	0.954	0.401	0.584	0.567	0.745	0.855
Depth-Facto [30] (AS)	23.560	0.677	0.514	0.149	0.055	0.014	0.991	0.995	0.997
Depth-Facto [30] (ToF)	23.530	0.679	0.517	0.166	0.028	0.025	0.979	0.987	0.992
Zip-NeRF [31]	23.559	0.646	0.459	0.737	0.376	0.379	0.273	0.626	0.748
Gaussian-Splatting [13]	24.457	0.693	0.417	0.521	0.210	0.148	0.588	0.834	0.916
Mip-Splatting [32]	24.258	0.693	0.416	0.530	0.212	0.153	0.592	0.829	0.912

Table 9: NVS Benchmark for scene08

Evaluation	RGB			Depth					
	PSNR $\uparrow$	SSIM $\uparrow$	LPIPS $\downarrow$	RSME $\downarrow$	Abs Rel $\downarrow$	Sqr Rel $\downarrow$	<1.25 <sup>1</sup> $\uparrow$	<1.25 <sup>2</sup> $\uparrow$	<1.25 <sup>3</sup> $\uparrow$
NeRFacto [30]	23.803	0.619	0.535	0.908	0.430	0.567	0.505	0.710	0.855
Depth-Facto [30] (AS)	24.849	0.629	0.517	0.121	0.048	0.009	0.988	0.995	0.999
Depth-Facto [30] (ToF)	24.913	0.632	0.513	0.097	0.023	0.008	0.983	0.992	0.998
Zip-NeRF [31]	26.584	0.629	0.367	0.304	0.153	0.060	0.735	0.971	0.983
Gaussian-Splatting [13]	25.140	0.639	0.416	0.389	0.153	0.084	0.720	0.908	0.961
Mip-Splatting [32]	25.214	0.640	0.415	0.385	0.149	0.082	0.732	0.907	0.960

Table 10: NVS Benchmark for scene09

Evaluation	RGB			Depth					
	PSNR $\uparrow$	SSIM $\uparrow$	LPIPS $\downarrow$	RSME $\downarrow$	Abs Rel $\downarrow$	Sqr Rel $\downarrow$	<1.25 <sup>1</sup> $\uparrow$	<1.25 <sup>2</sup> $\uparrow$	<1.25 <sup>3</sup> $\uparrow$
NeRFacto [30]	22.594	0.601	0.583	1.067	0.616	0.923	0.425	0.596	0.715
Depth-Facto [30] (AS)	23.273	0.610	0.571	0.097	0.037	0.006	0.990	0.996	0.999
Depth-Facto [30] (ToF)	23.029	0.607	0.572	0.128	0.030	0.021	0.974	0.983	0.986
Zip-NeRF [31]	23.734	0.603	0.433	0.484	0.270	0.175	0.406	0.766	0.884
Gaussian-Splatting [13]	24.038	0.626	0.427	0.364	0.160	0.084	0.709	0.898	0.958
Mip-Splatting [32]	24.091	0.627	0.428	0.364	0.160	0.086	0.704	0.891	0.954

Table 11: NVS Benchmark for scene10

Evaluation	RGB			Depth					
	PSNR $\uparrow$	SSIM $\uparrow$	LPIPS $\downarrow$	RSME $\downarrow$	Abs Rel $\downarrow$	Sqr Rel $\downarrow$	<1.25 <sup>1</sup> $\uparrow$	<1.25 <sup>2</sup> $\uparrow$	<1.25 <sup>3</sup> $\uparrow$
NeRFacto [30]	23.024	0.903	0.191	1.727	0.620	1.839	0.542	0.704	0.771
Depth-Facto [30] (AS)	23.685	0.908	0.203	0.190	0.067	0.017	0.991	0.999	1.000
Depth-Facto [30] (ToF)	23.705	0.909	0.194	0.163	0.030	0.016	0.980	0.993	0.998
Zip-NeRF [31]	36.385	0.942	0.119	0.343	0.137	0.052	0.769	0.993	1.000
Gaussian-Splatting [13]	26.637	0.928	0.231	0.450	0.143	0.099	0.770	0.923	0.963
Mip-Splatting [32]	26.648	0.929	0.229	0.431	0.138	0.091	0.774	0.928	0.968

Table 12: NVS Benchmark for scene11

Evaluation	RGB			Depth					
	PSNR $\uparrow$	SSIM $\uparrow$	LPIPS $\downarrow$	RSME $\downarrow$	Abs Rel $\downarrow$	Sqr Rel $\downarrow$	<1.25 <sup>1</sup> $\uparrow$	<1.25 <sup>2</sup> $\uparrow$	<1.25 <sup>3</sup> $\uparrow$
NeRFacto [30]	23.166	0.829	0.212	1.716	0.950	2.207	0.287	0.450	0.601
Depth-Facto [30] (AS)	27.510	0.889	0.178	0.330	0.122	0.102	0.958	0.977	0.983
Depth-Facto [30] (ToF)	27.695	0.886	0.174	0.589	0.151	0.246	0.858	0.894	0.928
Zip-NeRF [31]	33.866	0.894	0.121	0.563	0.242	0.217	0.574	0.821	0.895
Gaussian-Splatting [13]	28.360	0.928	0.199	0.691	0.273	0.249	0.474	0.715	0.828
Mip-Splatting [32]	28.299	0.929	0.200	0.715	0.289	0.266	0.439	0.669	0.804

## 5.2 SLAM

This benchmark compares several SLAM methods: NICE-SLAM [34], CO-SLAM [35], and Gaussian-SLAM [36], evaluated using Ground Truth (GT) data, AS (Active Stereo) sensor data, and TOF (Time of Flight) sensor data, highlighting the significant impact of sensor quality on SLAM performance.

NICE-SLAM achieves high-quality scene reconstruction by optimizing a hierarchical representation using pre-trained geometric priors [?]. However, it struggles with hole-filling. CO-SLAM further improves map completion by integrating smoothness and coherence priors into coordinate encodings [?]. On the other hand, Gaussian-SLAM efficiently seeds new Gaussians for newly explored areas and optimizes them online by organizing the scene into independently optimized sub-maps.

When using ground truth data, Gaussian-SLAM excels in both tracking and mapping performance, indicating a strong algorithm highly dependent on input quality. With the AS sensor, all SLAM methods exhibit some performance degradation due to the constant random noise in the depth sensor. Gaussian-SLAM shows substantial deterioration in both tracking and reconstruction performance, especially in scenes with motion blur, resulting in a higher ATE and reduced map completeness. However, CO-SLAM and NICE-SLAM demonstrate better resilience to the noisy depth input from the AS sensor, maintaining relatively higher map accuracy and completeness.

The TOF sensor data further challenges the SLAM methods since the depth quality is influenced by rapid motion. Gaussian-SLAM struggles significantly, even failing in scene07 due to unreliable photometric and geometric consistency. Its performance drops dramatically across all metrics. Conversely, leveraging hybrid scene representations, NICE-SLAM and CO-SLAM show better robustness towards the noisy depth input, with CO-SLAM maintaining higher map completion rates.

Table 13: SLAM Benchmarks for scene01.

Evaluation		Tracking		Mapping	
Methods	Depth	ATE↓ [cm]	Acc↓ [cm]	Comp↓ [cm]	Comp Ratio↑ [%]
NICE-SLAM [34]	GT	1.22	1.47	2.51	88.97
	AS	7.39	10.18	4.69	66.18
	ToF	7.39	17.01	7.03	65.34
CO-SLAM [35]	GT	3.22	1.48	1.46	96.06
	AS	9.18	6.29	3.40	78.19
	ToF	7.61	9.54	4.54	77.12
Gaussian-SLAM [36]	GT	0.86	0.65	0.76	99.64
	AS	9.18	21.53	3.73	74.62
	ToF	4.96	21.92	3.73	74.42

Table 14: SLAM Benchmarks for scene02.

Evaluation		Tracking		Mapping	
Methods	Depth	ATE↓ [cm]	Acc↓ [cm]	Comp↓ [cm]	Comp Ratio↑ [%]
NICE-SLAM [34]	GT	7.33	2.93	4.25	78.41
	AS	18.14	15.31	7.91	43.72
	ToF	5.15	18.20	6.84	69.02
CO-SLAM [35]	GT	3.50	1.49	1.54	97.04
	AS	13.27	27.33	13.95	36.21
	ToF	5.62	37.77	4.30	80.71
Gaussian-SLAM [36]	GT	1.83	1.15	1.16	99.06
	AS	17.50	25.75	10.50	33.48
	ToF	29.81	43.69	7.01	56.81

Table 15: SLAM Benchmarks for scene03.

Evaluation		Tracking	Mapping		
Methods	Depth	ATE $\downarrow$ [cm]	Acc $\downarrow$ [cm]	Comp $\downarrow$ [cm]	Comp Ratio $\uparrow$ [%]
NICE-SLAM [34]	GT	1.64	2.58	6.11	84.44
	AS	21.79	60.90	18.71	34.50
	ToF	8.19	31.26	12.70	61.87
CO-SLAM [35]	GT	5.55	2.53	1.21	98.07
	AS	18.32	55.16	13.43	39.49
	ToF	18.73	76.67	6.81	64.79
Gaussian-SLAM [36]	GT	5.35	4.64	1.35	96.98
	AS	13.02	120.85	7.66	49.35
	ToF	13.25	59.84	4.87	68.95

Table 16: SLAM Benchmarks for scene04, sequence00.

Evaluation		Tracking	Mapping		
Methods	Depth	ATE $\downarrow$ [cm]	Acc $\downarrow$ [cm]	Comp $\downarrow$ [cm]	Comp Ratio $\uparrow$ [%]
NICE-SLAM [34]	GT	9.89	3.77	9.83	62.29
	AS	45.89	22.20	17.31	26.03
	ToF	45.70	20.25	35.38	23.51
CO-SLAM [35]	GT	4.48	2.01	1.66	98.27
	AS	14.97	30.16	14.08	28.24
	ToF	13.94	97.31	12.54	31.56
Gaussian-SLAM [36]	GT	2.44	1.41	1.26	99.17
	AS	10.43	22.32	12.12	30.15
	ToF	60.36	33.70	16.93	29.58

Table 17: SLAM Benchmarks for scene04, sequence01.

Evaluation		Tracking	Mapping		
Methods	Depth	ATE $\downarrow$ [cm]	Acc $\downarrow$ [cm]	Comp $\downarrow$ [cm]	Comp Ratio $\uparrow$ [%]
NICE-SLAM [34]	GT	11.24	2.29	5.88	78.57
	AS	14.29	27.84	12.68	38.01
	ToF	14.13	20.95	10.18	48.43
CO-SLAM [35]	GT	8.02	2.21	2.13	94.37
	AS	13.74	67.72	15.30	26.15
	ToF	13.86	56.85	6.50	55.97
Gaussian-SLAM [36]	GT	2.53	1.51	1.28	99.68
	AS	35.27	24.03	9.92	37.61
	ToF	60.36	33.70	16.93	29.58

Table 18: SLAM Benchmarks for scene05.

Evaluation		Tracking	Mapping		
Methods	Depth	ATE $\downarrow$ [cm]	Acc $\downarrow$ [cm]	Comp $\downarrow$ [cm]	Comp Ratio $\uparrow$ [%]
NICE-SLAM [34]	GT	15.24	9.34	11.66	50.29
	AS	19.65	11.01	8.28	51.53
	ToF	22.48	24.04	15.53	33.80
CO-SLAM [35]	GT	5.64	2.93	2.78	87.64
	AS	16.37	19.19	8.26	49.41
	ToF	25.66	58.58	12.83	51.28
Gaussian-SLAM [36]	GT	17.90	2.92	2.78	87.63
	AS	15.02	19.25	8.27	49.43
	ToF	18.39	58.71	12.77	51.30



Table 19: SLAM Benchmarks for scene06.

Evaluation		Tracking		Mapping	
Methods	Depth	ATE $\downarrow$ [cm]	Acc $\downarrow$ [cm]	Comp $\downarrow$ [cm]	Comp Ratio $\uparrow$ [%]
NICE-SLAM [34]	GT	1.52	0.91	6.64	81.58
	AS	76.70	14.34	9.07	53.28
	ToF	114.70	27.12	13.33	40.22
CO-SLAM [35]	GT	3.23	1.10	1.10	99.16
	AS	8.05	12.59	4.21	71.79
	ToF	5.76	106.43	6.92	69.69
Gaussian-SLAM [36]	GT	1.26	0.77	0.79	99.92
	AS	6.24	19.84	4.44	66.16
	ToF	6.26	65.86	7.34	63.17

Table 20: SLAM Benchmarks for scene07.

Evaluation		Tracking		Mapping	
Methods	Depth	ATE $\downarrow$ [cm]	Acc $\downarrow$ [cm]	Comp $\downarrow$ [cm]	Comp Ratio $\uparrow$ [%]
NICE-SLAM [34]	GT	5.01	3.26	7.39	58.74
	AS	24.81	19.59	18.14	28.77
	ToF	5.96	15.60	8.67	54.41
CO-SLAM [35]	GT	5.22	1.74	1.76	97.57
	AS	14.07	21.75	14.83	33.20
	ToF	11.00	46.05	6.86	51.02
Gaussian-SLAM [36]	GT	1.50	1.30	1.29	99.55
	AS	151.90	28.53	14.04	34.61
	ToF	fail	fail	fail	fail

Table 21: SLAM Benchmarks for scene08.

Evaluation		Tracking		Mapping	
Methods	Depth	ATE $\downarrow$ [cm]	Acc $\downarrow$ [cm]	Comp $\downarrow$ [cm]	Comp Ratio $\uparrow$ [%]
NICE-SLAM [34]	GT	2.39	2.08	6.56	81.59
	AS	80.66	14.95	12.94	35.21
	ToF	11.41	11.51	9.99	57.69
CO-SLAM [35]	GT	3.64	1.61	1.68	96.88
	AS	17.86	23.03	12.87	34.23
	ToF	7.25	32.36	5.71	67.28
Gaussian-SLAM [36]	GT	2.25	1.31	1.35	99.22
	AS	19.46	21.68	10.73	36.49
	ToF	82.26	29.92	6.86	59.76

Table 22: SLAM Benchmarks for scene09.

Evaluation		Tracking		Mapping	
Methods	Depth	ATE $\downarrow$ [cm]	Acc $\downarrow$ [cm]	Comp $\downarrow$ [cm]	Comp Ratio $\uparrow$ [%]
NICE-SLAM [34]	GT	3.93	2.44	4.07	80.08
	AS	30.05	18.92	14.53	35.47
	ToF	22.15	24.98	31.79	20.78
CO-SLAM [35]	GT	2.29	1.66	1.69	97.64
	AS	19.39	17.50	10.74	45.87
	ToF	17.84	38.55	11.45	38.38
Gaussian-SLAM [36]	GT	0.75	1.07	1.12	99.53
	AS	4.28	14.46	6.61	53.73
	ToF	10.41	23.96	4.09	78.55

Table 23: **SLAM Benchmarks for scene10.**

Evaluation		Tracking	Mapping		
Methods	Depth	ATE↓ [cm]	Acc↓ [cm]	Comp↓ [cm]	Comp Ratio↑ [%]
NICE-SLAM [34]	GT	5.13	1.94	2.63	91.72
	AS	50.65	34.19	20.48	20.74
	ToF	18.95	25.41	12.89	36.88
CO-SLAM [35]	GT	2.28	1.67	1.59	97.65
	AS	242.38	75.08	21.55	22.98
	ToF	381.76	67.49	8.11	63.62
Gaussian-SLAM [36]	GT	16.06	6.66	4.40	72.90
	AS	56.91	77.00	19.55	16.58
	ToF	108.39	54.44	12.57	31.69

Table 24: **SLAM Benchmarks for scene11.**

Evaluation		Tracking	Mapping		
Methods	Depth	ATE↓ [cm]	Acc↓ [cm]	Comp↓ [cm]	Comp Ratio↑ [%]
NICE-SLAM [34]	GT	1.07	1.93	3.37	88.64
	AS	79.10	34.19	29.38	16.50
	ToF	11.86	16.00	8.72	52.62
CO-SLAM [35]	GT	3.06	1.96	1.70	97.92
	AS	51.78	40.79	19.51	17.23
	ToF	42.3	71.10	9.68	40.71
Gaussian-SLAM [36]	GT	7.21	3.66	2.80	85.46
	AS	119.20	60.03	33.32	14.11
	ToF	69.43	46.15	11.18	36.03

## 6 Licenses of Codes Used in Benchmarks

In this section, we show licenses of codes that are used in the benchmark for NVS (Tab. 25) and SLAM (Tab. 26). Note that our dataset uses the **MIT License**.

Table 25: **License Information of the NVS code Used in the Benchmark.**

Methods	NeRF(Depth)-Facto [30]	Zip-NeRF [31]	Gaussian-Splatting [13]	Mip-Splatting [32]
License	Apache-2.0	Apache-2.0	Inria and MPII	Inria and MPII

Table 26: **License Information of the SLAM code Used in the Benchmark.**

Methods	NICE-SLAM [34]	CO-SLAM [35]	Gaussian-SLAM [36]
License	Apache-2.0	Apache-2.0	MIT

## References

- [1] P. K. Nathan Silberman, Derek Hoiem and R. Fergus, “Indoor segmentation and support inference from rgb-d images,” in *ECCV*, 2012.
- [2] J. Sturm, N. Engelhard, F. Endres, W. Burgard, and D. Cremers, “A benchmark for the evaluation of rgb-d slam systems,” in *Proc. of the International Conference on Intelligent Robot Systems (IROS)*, Oct. 2012.
- [3] A. Dai, A. X. Chang, M. Savva, M. Halber, T. Funkhouser, and M. Nießner, “Scannet: Richly-annotated 3d reconstructions of indoor scenes,” in *Proc. Computer Vision and Pattern Recognition (CVPR), IEEE*, 2017.
- [4] A. Chang, A. Dai, T. Funkhouser, M. Halber, M. Niessner, M. Savva, S. Song, A. Zeng, and Y. Zhang, “Matterport3d: Learning from rgb-d data in indoor environments,” *International Conference on 3D Vision (3DV)*, 2017.
- [5] I. Armeni, A. Sax, A. R. Zamir, and S. Savarese, “Joint 2D-3D-Semantic Data for Indoor Scene Understanding,” *ArXiv e-prints*, Feb. 2017.
- [6] J. Straub, T. Whelan, L. Ma, Y. Chen, E. Wijmans, S. Green, J. J. Engel, R. Mur-Artal, C. Ren, S. Verma, A. Clarkson, M. Yan, B. Budge, Y. Yan, X. Pan, J. Yon, Y. Zou, K. Leon, N. Carter, J. Briales, T. Gillingham, E. Mueggler, L. Pesqueira, M. Savva, D. Batra, H. M. Strasdat, R. D. Nardi, M. Goesele, S. Lovegrove, and R. Newcombe, “The Replica dataset: A digital replica of indoor spaces,” *arXiv preprint arXiv:1906.05797*, 2019.
- [7] C. Yeshwanth, Y.-C. Liu, M. Nießner, and A. Dai, “Scannet++: A high-fidelity dataset of 3d indoor scenes,” in *Proceedings of the IEEE/CVF International Conference on Computer Vision*, 2023, pp. 12–22.
- [8] G. Baruch, Z. Chen, A. Dehghan, T. Dimry, Y. Feigin, P. Fu, T. Gebauer, B. Joffe, D. Kurz, A. Schwartz *et al.*, “Arkitscenes: A diverse real-world dataset for 3d indoor scene understanding using mobile rgb-d data,” *arXiv preprint arXiv:2111.08897*, 2021.
- [9] H. Jung, P. Ruhkamp, G. Zhai, N. Brasch, Y. Li, Y. Verdie, J. Song, Y. Zhou, A. Armagan, S. Ilic, A. Leonardis, N. Navab, and B. Busam, “On the importance of accurate geometry data for dense 3d vision tasks,” in *Proceedings of the IEEE/CVF Conference on Computer Vision and Pattern Recognition (CVPR)*, June 2023, pp. 780–791.
- [10] A. Szot, A. Clegg, E. Undersander, E. Wijmans, Y. Zhao, J. Turner, N. Maestre, M. Mukadam, D. Chaplot, O. Maksymets, A. Gokaslan, V. Vondrus, S. Dharur, F. Meier, W. Galuba, A. Chang, Z. Kira, V. Koltun, J. Malik, M. Savva, and D. Batra, “Habitat 2.0: Training home assistants to rearrange their habitat,” in *Advances in Neural Information Processing Systems (NeurIPS)*, 2021.
- [11] M. Deitke, W. Han, A. Herrasti, A. Kembhavi, E. Kolve, R. Mottaghi, J. Salvador, D. Schwenk, E. Vander-Bilt, M. Wallingford *et al.*, “Robothor: An open simulation-to-real embodied ai platform,” in *Proceedings of the IEEE/CVF conference on computer vision and pattern recognition*, 2020, pp. 3164–3174.
- [12] B. Mildenhall, P. P. Srinivasan, M. Tancik, J. T. Barron, R. Ramamoorthi, and R. Ng, “Nerf: Representing scenes as neural radiance fields for view synthesis,” *Communications of the ACM*, vol. 65, no. 1, pp. 99–106, 2021.

- [13] B. Kerbl, G. Kopanas, T. Leimkühler, and G. Drettakis, “3d gaussian splatting for real-time radiance field rendering,” *ACM Transactions on Graphics*, vol. 42, no. 4, July 2023. [Online]. Available: <https://repo-sam.inria.fr/fungraph/3d-gaussian-splatting/>
- [14] H. Jung, G. Zhai, S.-C. Wu, P. Ruhkamp, H. Schieber, G. Rizzoli, P. Wang, H. Zhao, L. Garattoni, S. Meier, D. Roth, N. Navab, and B. Busam, “Housecat6d – a large-scale multi-modal category level 6d object perception dataset with household objects in realistic scenarios,” in *Proceedings of the IEEE/CVF Conference on Computer Vision and Pattern Recognition (CVPR)*, June 2024.
- [15] K. S. Arun, T. S. Huang, and S. D. Blostein, “Least-squares fitting of two 3-d point sets,” *IEEE Transactions on Pattern Analysis and Machine Intelligence*, vol. PAMI-9, no. 5, pp. 698–700, 1987.
- [16] B. O. Community, *Blender - a 3D modelling and rendering package*, Blender Foundation, Stichting Blender Foundation, Amsterdam, 2018. [Online]. Available: <http://www.blender.org>
- [17] B. K. Horn, H. M. Hilden, and S. Negahdaripour, “Closed-form solution of absolute orientation using orthonormal matrices,” *Josa a*, vol. 5, no. 7, pp. 1127–1135, 1988.
- [18] J. L. Schönberger and J.-M. Frahm, “Structure-from-motion revisited,” in *Conference on Computer Vision and Pattern Recognition (CVPR)*, 2016.
- [19] J. L. Schönberger, E. Zheng, M. Pollefeys, and J.-M. Frahm, “Pixelwise view selection for unstructured multi-view stereo,” in *European Conference on Computer Vision (ECCV)*, 2016.
- [20] S. Peng, Y. Zhang, Y. Xu, Q. Wang, Q. Shuai, H. Bao, and X. Zhou, “Neural body: Implicit neural representations with structured latent codes for novel view synthesis of dynamic humans,” in *CVPR*, 2021.
- [21] H. Joo, T. Simon, X. Li, H. Liu, L. Tan, L. Gui, S. Banerjee, T. S. Godisart, B. Nabbe, I. Matthews, T. Kanade, S. Nobuhara, and Y. Sheikh, “Panoptic studio: A massively multiview system for social interaction capture,” *IEEE Transactions on Pattern Analysis and Machine Intelligence*, 2017.
- [22] M. Işık, M. Rünz, M. Georgopoulos, T. Khakhulin, J. Starck, L. Agapito, and M. Nießner, “Humanrf: High-fidelity neural radiance fields for humans in motion,” *ACM Transactions on Graphics (TOG)*, vol. 42, no. 4, pp. 1–12, 2023. [Online]. Available: <https://doi.org/10.1145/3592415>
- [23] W. Jiang, K. M. Yi, G. Samei, O. Tuzel, and A. Ranjan, “Neuman: Neural human radiance field from a single video,” 2022. [Online]. Available: <https://arxiv.org/abs/2203.12575>
- [24] M. Loper, N. Mahmood, J. Romero, G. Pons-Moll, and M. J. Black, “SMPL: A skinned multi-person linear model,” *ACM Trans. Graphics (Proc. SIGGRAPH Asia)*, vol. 34, no. 6, pp. 248:1–248:16, Oct. 2015.
- [25] B. L. Bhatnagar, C. Sminchisescu, C. Theobalt, and G. Pons-Moll, “Combining implicit function learning and parametric models for 3d human reconstruction,” in *European Conference on Computer Vision (ECCV)*. Springer, aug 2020.
- [26] ———, “Loopreg: Self-supervised learning of implicit surface correspondences, pose and shape for 3d human mesh registration,” in *Advances in Neural Information Processing Systems (NeurIPS)*, December 2020.
- [27] P. Wang, H. Jung, Y. Li, S. Shen, R. P. Srikant, L. Garattoni, S. Meier, N. Navab, and B. Busam, “Phocal: A multi-modal dataset for category-level object pose estimation with photometrically challenging objects,” in *Proceedings of the IEEE/CVF Conference on Computer Vision and Pattern Recognition (CVPR)*, June 2022, pp. 21 222–21 231.
- [28] X. Liu, S. Iwase, and K. M. Kitani, “Stereoobj-1m: Large-scale stereo image dataset for 6d object pose estimation,” in *Proceedings of the IEEE/CVF International Conference on Computer Vision*, 2021, pp. 10 870–10 879.
- [29] H. Wang, S. Sridhar, J. Huang, J. Valentin, S. Song, and L. J. Guibas, “Normalized object coordinate space for category-level 6d object pose and size estimation,” in *The IEEE Conference on Computer Vision and Pattern Recognition (CVPR)*, June 2019.
- [30] M. Tancik, E. Weber, E. Ng, R. Li, B. Yi, T. Wang, A. Kristoffersen, J. Austin, K. Salahi, A. Ahuja *et al.*, “Nerfstudio: A modular framework for neural radiance field development,” in *ACM SIGGRAPH 2023 Conference Proceedings*, 2023, pp. 1–12.
- [31] J. T. Barron, B. Mildenhall, D. Verbin, P. P. Srinivasan, and P. Hedman, “Zip-nerf: Anti-aliased grid-based neural radiance fields,” in *Proceedings of the IEEE/CVF International Conference on Computer Vision*, 2023, pp. 19 697–19 705.

- [32] Z. Yu, A. Chen, B. Huang, T. Sattler, and A. Geiger, “Mip-splatting: Alias-free 3d gaussian splatting,” *arXiv:2311.16493*, 2023.
- [33] R. Zhang, P. Isola, A. A. Efros, E. Shechtman, and O. Wang, “The unreasonable effectiveness of deep features as a perceptual metric,” in *CVPR*, 2018.
- [34] Z. Zhu, S. Peng, V. Larsson, W. Xu, H. Bao, Z. Cui, M. R. Oswald, and M. Pollefeys, “Nice-slam: Neural implicit scalable encoding for slam,” in *Proceedings of the IEEE/CVF Conference on Computer Vision and Pattern Recognition (CVPR)*, 2022.
- [35] H. Wang, J. Wang, and L. Agapito, “Co-slam: Joint coordinate and sparse parametric encodings for neural real-time slam,” in *CVPR*, 2023.
- [36] V. Yugay, Y. Li, T. Gevers, and M. R. Oswald, “Gaussian-slam: Photo-realistic dense slam with gaussian splatting,” 2023.
- [37] J. Sturm, N. Engelhard, F. Endres, W. Burgard, and D. Cremers, “A benchmark for the evaluation of rgb-d slam systems,” in *2012 IEEE/RSJ International Conference on Intelligent Robots and Systems*, Sep 2012. [Online]. Available: <http://dx.doi.org/10.1109/iros.2012.6385773>
- [38] E. Sucar, S. Liu, J. Ortiz, and A. J. Davison, “imap: Implicit mapping and positioning in real-time,” in *Proceedings of the IEEE/CVF International Conference on Computer Vision*, 2021, pp. 6229–6238.
- [39] D. Azinović, R. Martin-Brualla, D. B. Goldman, M. Nießner, and J. Thies, “Neural rgb-d surface reconstruction,” in *Proceedings of the IEEE/CVF Conference on Computer Vision and Pattern Recognition (CVPR)*, June 2022, pp. 6290–6301.
- [40] J. Kim, J. Kim, J. Na, and H. Joo, “Parahome: Parameterizing everyday home activities towards 3d generative modeling of human-object interactions,” *arXiv preprint arXiv:2401.10232*, 2024.